Improved Snow-Covered Forest Bidirectional Reflectance Model Incorporating Canopy-Intercepted Snow and Atmospheric Effects

Siyong Chen, Pengfeng Xiao, *Senior Member, IEEE*, Xueliang Zhang, *Senior Member, IEEE*, Hao Liu, Yunhan Wang, Liyang Sun, and Gaofei Yin, *Senior Member, IEEE*

***Abstract*— Snow-covered forests are widely distributed in middle- and high-latitude regions of the Northern Hemisphere and have significant impacts on global climate change and albedo feedback. However, knowledge of the radiative transfer mechanism in snow–canopy–atmosphere systems is insufficient. Existing bidirectional reflectance models often oversimplify, assuming that snow only persists on the floor, and neglect the interactions between the atmosphere and snow-covered forests. In our previous snow-covered forest bidirectional reflectance (SFBR) model, we considered ground snow, the concentration of soot pollution, needle leaf characteristics, and discontinuous canopy distributions. Furthermore, this study proposed an improved snow-covered forest bidirectional reflectance (SFBR2) model by considering canopy-intercepted snow (CIS) and atmospheric effects. Specifically, the SFBR2 model was constructed by a series of analytical models for CIS, ground snow (asymptotic radiative transfer (ART) snow model), soil [brightness shape moisture (BSM)], needle leaf [leaf incorporating biochemistry exhibiting reflectance and transmittance yields (LIBERTY)], canopy [two-layer version of four-stream scattering by arbitrarily inclined leaves (4SAIL2)], and atmosphere [simplified method for atmospheric correction (SMAC)], in which the CIS is parameterized by snow optical properties and two-stream theory, and the interaction between the atmosphere and snow-covered forests is optimized by a four-stream theory. It makes the model able to simulate the reflectance at the top of the canopy/atmosphere (TOC/TOA). Validations against 3-D large-scale remote sensing data and image simulation framework over heterogeneous 3-D scenes (LESS) model, unmanned aerial vehicle (UAV) observations, and MODIS data indicated a good consistency with SFBR2 model in the reflectance simulation. The established model has the ability to simulate the bidirectional reflectance of different snow-covered forest scenes whether CIS exists or not. Potential applications include satellite signal simulation, radiation mechanism analysis, and parameter inversion in snow-covered forests.**

***Index Terms*— Atmosphere, bidirectional reflectance, canopy-intercepted snow (CIS), radiative transfer, snow-covered forests.**

I. Introduction

SEASONAL snow is prevalent in coniferous forests of middle- and high-latitude regions, which occupy 1/5 of the snow region in the Northern Hemisphere [1]. In winter, snow-covered forests create strong heterogeneity in surface reflectance because snow has a high reflection, while canopy has strong absorption characteristics [2], and the reflectance differences can reach 30% when compared with snow-free forests [3], [4]. Moreover, the variations of snow-covered forests are connected to the Earth's surface albedo and greatly influence biophysical effects [5], radiation budget [6], [7], and carbon cycling [8]. Optical remote sensing, which can identify snow areas [9], retrieve snow albedo [10], and extract snow/vegetation phenology [11], is an important way to monitor snow-covered forests. However, the applied methods do not provide a detailed description of relation between snow–canopy parameters and bidirectional reflectance because a deep understanding of the radiation mechanism in snow-covered forests is deficient. Therefore, further study on the bidirectional reflectance distribution function (BRDF) and the establishment of a forward model for snow-covered forests are urgently needed.

The canopy reflectance model may help simulate the BRDF of snow-covered forests with different scene complexities. Such models include radiative transfer, geometric optical, hybrid geometric optical-radiative transfer (GORT), and 3-D computer simulation models [12], [13], which are well developed and widely applied to soil-canopy systems [14]. The presence of snow is the main challenge in applying current canopy reflectance models to forests because snow can be distributed in the above and bottom canopy, and the multiple

Manuscript received 18 February 2024; revised 10 May 2024 and 24 June 2024; accepted 5 July 2024. Date of publication 15 July 2024; date of current version 30 July 2024. This work was supported in part by the National Natural Science Foundation of China under Grant 42171307; and in part by the "GeoX" Interdisciplinary Research Funds for the Frontiers Science Center for Critical Earth Material Cycling, Nanjing University. *(Corresponding author: Pengfeng Xiao.)*

Siyong Chen, Xueliang Zhang, Hao Liu, Yunhan Wang, and Liyang Sun are with Jiangsu Provincial Key Laboratory of Geographic Information Science and Technology, Key Laboratory for Land Satellite Remote Sensing Applications of Ministry of Natural Resources, School of Geography and Ocean Science, Nanjing University, Nanjing, Jiangsu 210023, China.

Pengfeng Xiao is with Jiangsu Provincial Key Laboratory of Geographic Information Science and Technology, Key Laboratory for Land Satellite Remote Sensing Applications of Ministry of Natural Resources, School of Geography and Ocean Science, Nanjing University, Nanjing, Jiangsu 210023, China, and also with Jiangsu Center for Collaborative Innovation in Geographical Information Resource Development and Application, Nanjing, Jiangsu 210023, China (e-mail: xiaopf@nju.edu.cn).

Gaofei Yin is with the Faculty of Geosciences and Environmental Engineering, Southwest Jiaotong University, Chengdu, Sichuan 610031, China.

Digital Object Identifier 10.1109/TGRS.2024.3427818

scattering between canopy and snow is extremely complex. Moreover, the forward scattering characteristics of snow, needle leaf spectral characteristics, vegetation distributions, fractional snow cover (FSC) on the land surface, and atmospheric effects all have different influences on the BRDF simulation of snow-covered forests [4], [15].

Efforts on BRDF modeling of snow-covered forests in previous studies can be divided into single-directional simulations and bidirectional simulations. For single-directional simulations, the model can be used only for simulating nadir reflectance or albedo. For example, linear mixing models simulate snow-covered forest reflectance based on a linear combination of ground component reflectance and area rates [16]; the representative algorithms include snow-covered forest reflectance model (SnowFor) [17], MODIS snow-covered area and grain size algorithm (MODSCAG) [10], and multiple endmember spectral mixture analysis algorithm (MESMA) [18]; and the lack of forward simulation of the component area ratio is the primary distinction with geometric optical model. Moreover, linear mixing models are unable to consider multiple-scattering effects. The GeoSail canopy reflectance model [19] was combined with a two-stream theory-based snow model [20] to simulate the nadir reflectance of snow-covered forests [21], which is primarily used to improve the accuracy of snow mapping in forested areas. Some researchers simulated the albedo of snow-covered forests by establishing the relation between P-theory and leaf area index (LAI) [22], [23], and the multiple scatters between snow and canopy were well parameterized by a spectral invariant [24]. Such a model can be effectively used for albedo simulation but not as a bidirectional reflectance model for snow-covered forests.

For bidirectional simulation, a zeroth-order radiative transfer model was used to simulate the reflectance of conifer forests with full snow cover on the ground [25], and this model is an improved version of the snow-covered area model (SCAmod) [26], [27]. The reflectance of snow-covered forests was simulated by snow reflectance, forest reflectance, and two-way canopy transmissivity, without considering shading effects and multiple-scattering characteristics. The snow model, properties spectra (PROSPECT) broadleaf model [28], and GORT canopy model [29], [30] were also combined to simulate reflectance and investigate the influence of view angles on snow mapping in forested areas [31], [32]. Such a snow model is parameterized by snow grain size based on a two-stream theory [20] or Monte Carlo ray tracing [33], and the crown is assumed to be a discrete ellipsoid distributed randomly on flat ground with FSC. To further consider the anisotropic reflection characteristics of snow, concentration of soot pollution within snow, needle leaf characteristics, discontinuous canopy distribution, and topographic effects, our previous snow-covered forest bidirectional reflectance (SFBR) model [15] coupled leaf incorporating biochemistry exhibiting reflectance and transmittance yields (LIBERTY) [34], asymptotic radiative transfer (ART) snow model [35], a new canopy geometric optical model for sloping terrains (GOST2) [36], and four-stream scattering by arbitrarily inclined leaves (4SAIL) [37] to simulate the BRDF of snow-covered forests, while the 3-D large-scale remote sensing data and image simulation framework over heterogeneous 3-D scenes (LESS) [38] was employed to verify the effectiveness of the simulation results.

The above studies have made milestone contributions to promoting accurate simulations of BRDF in snow-covered forests, but challenges and uncertainties persist. In natural conditions, snow is not just distributed on the floor. Snow intercepted by canopy is a general phenomenon in forest areas [3], [39], and this proportion can reach 60% of the total snowfall [40]. The disordered distribution of canopy-intercepted snow (CIS) alters the scattering, absorption, and reflection characteristics of the original canopy [41], [42], but CIS has not been considered in BRDF simulations. Moreover, previous simulations of snow-covered forest reflectance were limited to the bottom of atmosphere. Considering that atmospheric effects and establishing a forward model for snow–canopy–atmosphere systems will be convenient for directly inverting snow-covered forest parameters based on satellite data, this viewpoint has been proven in snow or soil-canopy environments [43], [44].

Therefore, we aim to develop an SFBR model with consideration of CIS and simulate the BRDF at the top of canopy/atmosphere (TOC/TOA). Moreover, the anisotropic reflection characteristics of snow, concentration of soot pollution, FSC, and needle leaf characteristics are all integrated to depict the complex snow-covered forest scenes and quantify the impact of structural parameters on BRDF. This improved snow-covered forest bidirectional reflectance (SFBR2) model can output bidirectional reflectance flexibly and efficiently. More details about the modeling process of the SFBR2 model are given in Section II. In Section III, model validation is performed based on the 3-D LESS model, unmanned aerial vehicle (UAV)-based multiangle reflectance, and MODIS data, and a global and local sensitivity analysis to the TOC/TOA reflectance is also conducted. Sections IV and V present the discussion and conclusions, respectively.

II. SFBR2 Model

A. Overview

A system of snow-covered forests consists of three layers: the fractional coverage of snow and soil in the understory, the canopy and intercepted snow at the intermediate layer, and the atmosphere at the top layer. To balance model accuracy and efficiency for better application in the future, the SFBR2 model is constructed from a series of analytical models, including the ART snow anisotropic reflectance model [45], brightness-shape-moisture (BSM) soil isotropic reflectance model [46], LIBERTY needle leaf optical properties model [34], two-layer version of 4SAIL (4SAIL2) canopy reflectance model [37], and modified simplified method for atmospheric correction (SMAC) atmospheric radiative transfer model [44]. Modifications include that: 1) the reflectance/transmittance of CIS is parameterized by a two-stream theory; 2) the BSM model is combined with the Walthall model [47] to simulate soil anisotropic reflectance; and 3) the interaction between the atmosphere and snow-covered forests is optimized by a four-stream theory. The interactions between snow-covered forests and solar radiation are shown in Fig. 1, and the model

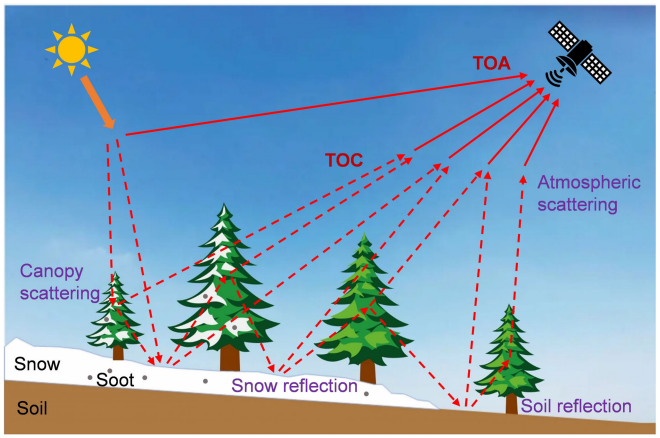

Fig. 1. Interaction between snow-covered forests and solar radiation. The white snow partly covers the ground surface, with some intercepted by the canopy; gray dots represent soot pollutions in the snow; and the solid and dashed lines depict the process of solar radiation passing through the atmosphere, canopy, snow, and soil, undergoing scattering and reflection before ultimately being received by a sensor.

parameters and coupling process are summarized in Table I and Fig. 2. Both the TOC and TOA reflectance can be output at different viewing angles.

B. Components of Snow-Covered Forests

1) Canopy-Intercepted Snow: Until now, CIS has not been considered in the BRDF model of snow-covered forests, and how to parameterize optical properties and simulate the radiative transfer of CIS has always been a challenge. Under natural conditions, CIS mainly adheres to leaves; thus, we assume that CIS is a large leaf with a certain thickness, and then, reflectance and transmittance of CIS can be simulated by parameterization of snow optical properties and radiative transfer models.

The inherent optical properties for ice and snow (ISIOP) tool [48] based on the Mie theory was used to calculate the optical properties of snow (single-scattering albedo ω, effective optical depth τ, and asymmetry factor g)

$$\omega = \frac{Q_a}{Q_a + Q_b}; \quad \tau = \pi a_{\text{ef}}^2 N H_{\text{sno}}(Q_a + Q_b); \quad g = g_0^{(1-Q_a)^{0.6}} \tag{1}$$

where g_0 is the asymmetry factor for nonabsorbing particles and is equal to 0.89 for snow and Q_a and Q_b are the absorption and scattering efficiency of snow, respectively,

$$Q_a = 0.94\left[1 - \exp\left(Q_a'/0.94\right)\right]; \quad Q_b = 2 - Q_a \tag{2}$$

$$Q_a' = \frac{16\pi a_{\text{ef}}}{3\lambda}\frac{m}{n}\left[n^3 - \left(n^2 - 1\right)^{3/2}\right]; \quad Q_b' = 2 \tag{3}$$

where a_{ef} is the snow grain size; λ is the wavelength; H_{sno} is the thickness of the snow; and n and m are the real and imaginary parts of the refractive index, respectively. The number of snow particles per unit volume is $N = (1/(4\pi a_{\text{ef}}^3/3))\rho_s/\rho_i$, where ρ_i and ρ_s are the densities of pure ice and snow, respectively. In the real environment, soot pollution has a notable influence on the absorptivity of snow, and the absorption efficiency of soot pollution can be calculated by the Mie theory $Q_a^{\text{soot}} = 3.2\pi a_{\text{soot}}\zeta/3\lambda$ [49], where the optimal value of the snow shape factor $\zeta = 1.6$ is retrieved from a simulation

TABLE I
PARAMETERS USED IN THE SFBR2 MODEL

Element	Parameter	Unit	Default value	Range
Atmosphere	Air pressure (Pa)	hPa	1013.25	500–1300
	Aerosol optical depth at 550 nm (AOD)	-	0.325	0–1.8
	Ozone content (U_{O3})	cm-atm	0.35	0–0.8
	Water vapour (U_{H2O})	g cm^{-2}	1.41	0–8.5
Leaf	Cell diameter (D)	μm	40	20–100
	Leaf thickness (H_{lea})	-	1.6	1–10
	Intercellular air space (X_u)	-	0.045	0.01–0.1
	Baseline absorption (A_{bas})	-	0.0005	-
	Albino absorption (A_{alb})	-	2	0–4
	Chlorophyll content (C_{ab})	mg m^{-2}	200	0–600
	Lignin content (C_l)	g m^{-2}	40	10–80
	Nitrogen content (C_n)	g m^{-2}	1	0.3–2
	Water content (C_w)	g m^{-2}	100	0–500
Canopy	Leaf angle distribution (LAD)	-	Spherical	Spherical
	Total (leaf + snow) area index(TAI)	-	4.5	0–7
	Hot spot (q)	-	0.01	0–0.2
	Fractional canopy-intercepted snow (F_{CIS})	-	0	0–0.8
	Thickness of canopy-intercepted snow (H_{sno})	mm	20	1–100
	Dissociation factor (Diss)	-	0.1	0–1
	Vertical crown cover fraction (C_v)	-	0.55	0–1
	Tree shadow factor (Zeta)	-	0.5	0.1–0.9
Snow	Snow grain size (a_{ef})	μm	500	100–2000
	Concentration of soot pollution (C_{soot})	ppb	0	0–2000
	Fractional snow cover in land surface (FSC)	-	1	0–1
Soil	Soil brightness (B)	-	0.3	0–0.5
	Soil spectral latitude (lat)	-	0	–30–30
	Soil spectral longitude (lon)	-	100	80–120
	Soil moisture content (SMC)	-	20	5–55
Geometry	Solar zenith angle (θ_s)	deg	40	0–70
	Solar azimuth angle (φ_s)	deg	0	0–360
	View zenith angle (θ_v)	deg	0	0–70
	View azimuth angle (φ_v)	deg	180	0–360

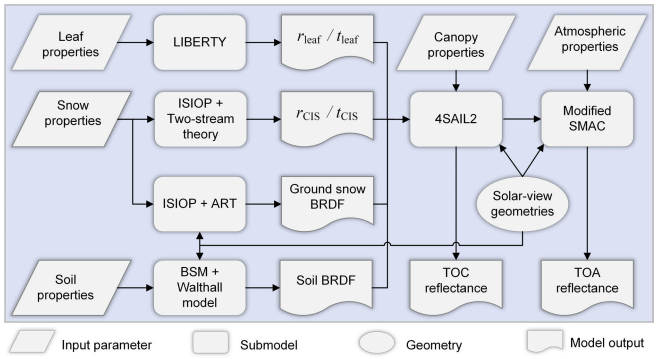

Fig. 2. Flowchart of the SFBR2 model. r_{leaf} and t_{leaf} are the reflectance and transmittance of leaf, respectively; and r_{CIS} and t_{CIS} are the reflectance and transmittance of CIS, respectively.

experiment [50] and a_{soot} is the grain size of soot pollution. Therefore, the effects of soot pollution are considered for snow by adding Q_a^{soot} weighted by concentration to Q_a in (2).

After completing the calculation of the optical properties of snow, the effects of CIS are simulated by the delta-Eddington method and two-stream theory [51], which have been successfully applied to calculate pure snow albedo [20]. Specifically, τ, ω, and g are transformed to $\tau^* = (1-\omega g^2)\tau$, $\omega^* = (1-g^2)\omega/(1-g^2\omega)$, and $g^* = g/(1+g)$ for handling asymmetric phase functions, and the reflectance/transmittance of CIS ($r_{\text{CIS}}/t_{\text{CIS}}$) is obtained by solving equations under simplified boundary conditions [51]

$$\begin{aligned} r_{\text{CIS}} = {} & \frac{\omega^*}{\left(1-k^2\mu_0^2\right)\left[(k+\gamma_1)e^{k\tau^*}+(k-\gamma_1)e^{-k\tau^*}\right]} \\ & \times \left[(1-k\mu_0)(\alpha_2+k\gamma_3)e^{k\tau^*}\right. \\ & -(1+k\mu_0)(\alpha_2-k\gamma_3)e^{-k\tau^*} \\ & \left.-2k(\gamma_3-\alpha_2\mu_0)e^{-\tau^*/\mu_0}\right] \end{aligned} \tag{4}$$

$$\begin{aligned} t_{\text{CIS}} = {} & e^{-\tau^*/\mu_0} - \frac{\omega^* e^{-\tau^*/\mu_0}}{\left(1-k^2\mu_0^2\right)\left[(k+\gamma_1)e^{k\tau^*}+(k-\gamma_1)e^{-k\tau^*}\right]} \\ & \times \left[(1+k\mu_0)(\alpha_1+k\gamma_4)e^{k\tau^*}\right. \\ & -(1-k\mu_0)(\alpha_1-k\gamma_4)e^{-k\tau^*} \\ & \left.-2k(\gamma_4-\alpha_1\mu_0)e^{\tau^*/\mu_0}\right] \end{aligned} \tag{5}$$

where

$$\alpha_1 = \gamma_1\gamma_4+\gamma_2\gamma_3; \quad \alpha_2 = \gamma_1\gamma_3+\gamma_2\gamma_4; \quad k = \sqrt{\gamma_1^2-\gamma_2^2} \tag{6}$$

$$\begin{aligned} & \gamma_1 = \left[7-\omega^*(4+3g^*)\right]/4; \quad \gamma_2 = -\left[1-\omega^*(4-3g^*)\right]/4 \\ & \gamma_3 = (2-3\mu_0 g^*)/4; \quad \gamma_4 = 1-\gamma_3; \quad \mu_0 = 1. \end{aligned} \tag{7}$$

2) Ground Snow: Snow is a non-Lambertian reflector on the land surface, and field measurements reflect obvious forward reflection characteristics [52]. In previous studies, many methods based on radiative transfer and photon tracing were developed to simulate the snow BRDF [53], in which the ART model [35], [54], developed based on the nonabsorbing, semi-infinite snow layer assumption, was widely used for snow modeling and retrieval studies. The ART can calculate the four reflectance factors of snow in an exponential form flexibly

$$\begin{aligned} R^{\text{snow}} &= \begin{bmatrix} r_{\text{sd}}^{\text{snow}} & r_{\text{dd}}^{\text{snow}} \\ r_{\text{so}}^{\text{snow}} & r_{\text{do}}^{\text{snow}} \end{bmatrix} \\ &= \begin{bmatrix} \exp(-yK_s) & \exp(-y) \\ r_0\exp(-yK_sK_v/r_0) & \exp(-yK_v) \end{bmatrix} \end{aligned} \tag{8}$$

where r_0 is the reflectance of the nonabsorbing medium; and K_s and K_v are the escape functions for different solar and view zenith angles, respectively, and these are angle-related variables that are well described in the previous study [45]. $r_{\text{so}}^{\text{snow}}$, $r_{\text{sd}}^{\text{snow}}$, $r_{\text{do}}^{\text{snow}}$, and $r_{\text{dd}}^{\text{snow}}$ are the bidirectional, directional-hemispherical, hemispherical-directional, and bihemispherical reflectances of snow, respectively.

The intermediate variable y can be parameterized by the optical properties of snow $y = 4((1-\omega)/[3(1-g)])^{1/2}$ [55] when snow is assumed to constitute a semi-infinite medium layer in the geometric optic theory [56]. However, the semi-infinite assumption cannot be applied to CIS with a specific thickness. Thus, the asymmetry factor g and single-scattering albedo ω are also used in combination with the ISIOP tool for simulation, which maintains the consistency of optical properties between CIS and ground snow.

3) Soil: Soil simulations are not a core component of snow-covered forests, but land surface mixtures of FSC and soil prevail during snow accumulation and melting periods. We employed the BSM model for simulating soil reflectance, which calculates the spectra by linear combination of dry (ρ_{dry}) and wet (ρ_{wet}) soil reflectance [44]

$$\rho_{\text{soil}} = P(l=0)\cdot\rho_{\text{dry}} + \sum_{k=1}^{\infty} P(l)\cdot\rho_{\text{wet}}(l) \tag{9}$$

where l represents the number of elementary water films, $P(l=0)$ is the proportion of dry soil and $P(l) = e^{-((\text{SMC}-5)/25)}\cdot((\text{SMC}-5)/25)^l/l!$, and SMC represents the soil moisture content. The wet soil reflectance is described by the water film coating approach [57], which assumes that wet soil is composed of dry soil and l thin water layer; thus, ρ_{wet} can be simulated by inputting ρ_{dry} and SMC.

The core of BSM model is spectra simulation of dry soil by two shape parameters (lat and lon) [46], brightness (B), and three spectral vectors [58]

$$\rho_{\text{dry}} = \begin{bmatrix} G_1 & G_2 & G_3 \end{bmatrix} \begin{bmatrix} B\sin(\text{lat}) \\ B\cos(\text{lat})\sin(\text{lon}) \\ B\cos(\text{lat})\cos(\text{lon}) \end{bmatrix} \tag{10}$$

where G_1–G_3 are the dry soil spectral vectors derived from 23 871 soil spectra worldwide by the matrix decomposition algorithm. These global soil spectral vectors are more representative than spectral vectors in the Price model [59], and it only used local soil spectra as the training dataset.

In the BSM model, the anisotropic characteristics of soil reflections are not considered, but soil BRDF plays a dominant role in sparse forests when sensors observe the Earth at different viewing angles [60], [61]. Thus, we combined the BSM model with the Walthall soil model [47], [62], which is widely used in parameter inversion for soil-canopy systems [63], [64], to calculate the bidirectional reflectance of soil

$$r_{\text{so}}^{\text{soil}} = \frac{\rho_{\text{soil}}}{p_0}\left[a\left(\theta_s^2+\theta_v^2\right)+b\theta_s^2\theta_v^2+c\theta_s\theta_v\cos(\varphi)+d\right] \tag{11}$$

where a, b, c, and d are −4.3, 7.702, 7.363, and 16.41, respectively; p_0 equals 13.76; θ_s and θ_v are the solar and view zenith angles, respectively; and φ is the relative azimuth angle. The soil directional-hemispherical reflectance $r_{\text{sd}}^{\text{soil}}$, hemispherical-directional reflectance $r_{\text{do}}^{\text{soil}}$, and bihemispherical reflectance $r_{\text{dd}}^{\text{soil}}$ can be easily integrated by (11). Thus, the soil reflectance factors can be represented as a matrix

$$R^{\text{soil}} = \begin{bmatrix} r_{\text{sd}}^{\text{soil}} & r_{\text{dd}}^{\text{soil}} \\ r_{\text{so}}^{\text{soil}} & r_{\text{do}}^{\text{soil}} \end{bmatrix}. \tag{12}$$

4) Leaf, Canopy, and Atmosphere: LIBERTY adopts a radiative transfer theory to determine leaf reflectance/transmittance ($r_{\text{leaf}}/t_{\text{leaf}}$) [34], [65]. This approach is suitable for simulating needle leaf optical properties

because it considers leaves as finite dimensions in the cross-light direction. The LIBERTY and canopy radiative transfer model (SAIL) have been coupled to reflectance simulation of coniferous forests [66]. 4SAIL2, the latest version of the SAIL model, is suitable for two-layer canopy structures and can effectively consider two different leaves [37]. Thus, it can be employed to handle the radiative transfer process of canopy with mixed leaves and CIS.

In the 4SAIL2 model, the clumping effects of the canopy were considered by the forest–light interaction model [67] with the parameters of vertical canopy coverage (C_v) and tree shadow factor (Zeta). Thus, the areas of sunlit canopy (F_{cs}), sunlit floor (F_{os}), shaded canopy (F_{cd}), and shaded floor (F_{od}) can be acquired when $C_v > 0$. These proportions are important for combining the reflectance of snow and canopy. Moreover, we used the total (leaf + snow) area index (TAI) to describe the structural characteristics of snow-covered forests TAI = SAI+LAI, where SAI and LAI are the snow area index (SAI) and LAI, respectively. The specific simulation process is given as follows.

1) Based on the reflectance/transmittance of leaf and CIS, the input parameters of reflectance (r_1, r_2), transmittance (t_1, t_2), and total area index (TAI_1, TAI_2) in each layer are calculated as

$$\begin{aligned} r_1 &= [1-(1-\text{Diss})(1-F_{\text{CIS}})]r_{\text{CIS}} \\ &\quad +(1-\text{Diss})(1-F_{\text{CIS}})r_{\text{leaf}} \\ t_1 &= [1-(1-\text{Diss})(1-F_{\text{CIS}})]t_{\text{CIS}} \\ &\quad +(1-\text{Diss})(1-F_{\text{CIS}})t_{\text{leaf}} \\ r_2 &= (1-\text{Diss})F_{\text{CIS}}r_{\text{CIS}}+[1-(1-\text{Diss})F_{\text{CIS}}]r_{\text{leaf}} \\ t_2 &= (1-\text{Diss})F_{\text{CIS}}t_{\text{CIS}}+[1-(1-\text{Diss})F_{\text{CIS}}]t_{\text{leaf}} \\ \text{TAI}_1 &= F_{\text{CIS}}\text{TAI} \\ \text{TAI}_2 &= (1-F_{\text{CIS}})\text{TAI} \end{aligned} \tag{13}$$

where F_{CIS} = SAI/TAI and Diss represents the dissociation factor. When Diss equals unity, all CIS is in the top layer, while all leaves are in the bottom layer. When Diss equals zero, CIS and leaves are homogeneously mixed over both layers.

2) r_1/t_1, r_2/t_2, and TAI_1/TAI_2 are input into 4SAIL to simulate the canopy scattering matrix for each layer, and the results of the two layers are combined.

3) The clumping effect is applied to the vegetation canopy to obtain the final canopy scattering matrix (14), as shown at the bottom of the next page, where the subscripts of the left matrix indicate the top (t), bottom (b), upward (u), and downward (d); the subscripts of the right matrix indicate the solar (s), observed (o), and diffuse (d) radiation fluxes; and the variables with superscripts c′ and c represent the simulated results of steps 2 and 3, respectively. R and T represent the reflectance and transmittance matrices, respectively, while ρ and τ denote their respective reflectance and transmittance values, respectively; and C_o and C_s are the projected canopy coverages in the view and sunlit directions, respectively.

For the atmosphere effects, the SMAC model is utilized to simulate the radiative transfer process [68], this process predetermines the semiempirical fitting functions, and the coefficients are calibrated by the 6S model [69] for a given spectral band; a fast computing speed can be achieved. The original SMAC model is only used to couple Lambertian surfaces, but the modified SMAC can be used for anisotropic surfaces by separating diffuse and direct atmosphere transmittances [44]. Thus, the scattering matrix of the atmosphere can be acquired

$$\begin{bmatrix} T_d^a & R_b^a \\ R_t^a & T_u^a \end{bmatrix} = \begin{bmatrix} \tau_{ss}^a & 0 & 0 & 0 \\ \tau_{sd}^a & \tau_{dd}^a & \rho_{dd}^a & 0 \\ \rho_{sd}^a & \rho_{dd}^a & \tau_{dd}^a & 0 \\ \rho_{so}^a & \rho_{do}^a & \tau_{do}^a & \tau_{oo}^a \end{bmatrix} \tag{15}$$

where R, T, τ, and ρ are consistent with (14) but are applied for the atmosphere. The superscript "a" indicates atmospheric variables.

C. TOC and TOA Reflectance Simulation

Before simulating the TOC reflectance, the solar zenith/azimuth angle (θ_s/φ_s) and view zenith/azimuth angle (θ_v/φ_v) are input into the ART snow model and BSM soil model to simulate the reflection matrix of the land surface

$$R^l = \begin{bmatrix} r_{sd}^l & r_{dd}^l \\ r_{so}^l & r_{do}^l \end{bmatrix} = \text{FSC}\cdot R^{\text{snow}} + (1-\text{FSC})\cdot R^{\text{soil}} \tag{16}$$

where FSC is the fractional snow cover. The superscript "l" indicates the variables of the land surface.

Furthermore, the interaction between the land surface and canopy is simulated by the four-stream theory [70]. The surface reflectance R^l and the scatter matrix of the canopy R_t^c, R_b^c, T_d^c, and T_u^c are the main input parameters. The clumping effects of the canopy and intercepted snow are effectively considered in the 4SAIL2 model, which indicates that radiation through the canopy effectively includes the contribution of the nonvegetation-covered part, and radiation reflected by the canopy includes the contribution of intercepted snow. Finally, the TOC reflection matrix is expressed as

$$R^c = \begin{bmatrix} r_{sd}^c & r_{dd}^c \\ r_{so}^c & r_{do}^c \end{bmatrix} = R_t^c + T_u^c\left[I - R_b^c R^l\right]^{-1} R^l T_d^c \tag{17}$$

where

$$\begin{aligned} r_{so}^c &= \rho_{so}^c + \tau_{ssoo}^c r_{so}^l \\ &\quad + \frac{\left(\tau_{ss}^c r_{sd}^l + \tau_{sd}^c r_{dd}^l\right)\tau_{do}^c + \left(\tau_{sd}^c + \tau_{ss}^c r_{sd}^l \rho_{dd}^c\right) r_{do}^l \tau_{oo}^c}{1 - r_{dd}^l \rho_{dd}^c} \\ r_{do}^c &= \rho_{do}^c + \frac{\tau_{dd}^c\left(r_{dd}^l \tau_{do}^c + r_{do}^l \tau_{oo}^c\right)}{1 - r_{dd}^l \rho_{dd}^c} \\ r_{sd}^c &= \rho_{sd}^c + \frac{\left(\tau_{ss}^c r_{sd}^l + \tau_{sd}^c r_{dd}^l\right)\tau_{dd}^c}{1 - r_{dd}^l \rho_{dd}^c} \\ r_{dd}^c &= \rho_{dd}^c + \frac{\tau_{dd}^c r_{dd}^l \tau_{dd}^c}{1 - r_{dd}^l \rho_{dd}^c} \end{aligned} \tag{18}$$

where $\tau_{ssoo}^c = F_{cd}\tau_{ssoo}^{c'} + F_{cs}\tau_{oo}^{c'} + F_{od}\tau_{ss}^{c'} + F_{os}$, which better accounts for shadowing between trees [71], and $\tau_{ssoo}^{c'}$ is the bidirectional gap probability.

At the bottom of the atmosphere, the reflectance observed by satellites includes direct and diffuse fluxes. Thus, the TOC

reflectance is weighted by the atmospheric transmittances τ_{ss}^{a} and τ_{sd}^{a}

$$r^{toc} = \frac{\tau_{ss}^{a} r_{so}^{c} + \tau_{sd}^{a} r_{do}^{c}}{\tau_{ss}^{a} + \tau_{sd}^{a}} = (1 - \mathrm{SKYL}) r_{so}^{c} + \mathrm{SKYL} r_{do}^{c} \quad (19)$$

where SKYL is the fraction of diffuse skylight.

TOA reflectance can also be simulated similarly, but the snow–canopy system acts as the background and atmosphere layer on the top. At the atmosphere's upper boundary, the solar radiation consists solely of direct flux, and thus, the TOA reflectance observed by satellites can be expressed as a bidirectional reflectance factor

$$r^{toa} = \rho_{so}^{a} + \tau_{ss}^{a} r_{so}^{c} \tau_{oo}^{a} + \frac{\left(\tau_{ss}^{a} r_{sd}^{c} + \tau_{sd}^{a} r_{dd}^{c}\right) \tau_{do}^{a} + \left(\tau_{sd}^{a} + \tau_{ss}^{a} r_{sd}^{c} \rho_{dd}^{a}\right) r_{do}^{c} \tau_{oo}^{a}}{1 - r_{dd}^{c} \rho_{dd}^{a}}. \quad (20)$$

III. Model Validation and Analysis

A. Validation Methods and Data

Comparisons with 3-D radiative transfer models, UAV observations, and MODIS data are adopted in our study to estimate the model's effectiveness. In theory, the 3-D model yields highly accurate reflectance simulations for discontinuous forests but at low running speeds, and thus, the 3-D model is an excellent tool for model validation. The 3-D LESS model is a remote sensing simulation framework based on the ray-tracing technique [38] and is widely used to validate analytical models about directional brightness temperatures and reflectance simulations in soil-canopy systems [72], [73]. In our previous study, the ART snow model and LIBERTY needleaf model were coupled to the LESS model [15], which makes LESS also have ability to validate bidirectional reflectance of snow-covered forests. Thus, the SFBR2 model can be estimated via the LESS with the same input parameters.

The LESS model simulation involves several key steps. Initially, a 3-D landscape for flat ground is created, and the crowns are randomly distributed in a region of 100 × 100 m (Fig. 3). Next, the essential parameters, including the optical characteristics of snow and leaves and the solar-view geometry, are input to the simulation. Finally, the bidirectional reflectance is generated using either an orthographic or photon tracing pattern. The LESS model is also coupled with the 6S atmosphere model [69] and can be easily utilized in the graphic user interface tool. Thus, both TOC and TOA reflectance can be estimated by the LESS in different scenes of snow-covered forests. Meanwhile, the SFBR models are also compared with the LESS model in terms of reflectance simulation to comprehensively assess the performance of SFBR2.

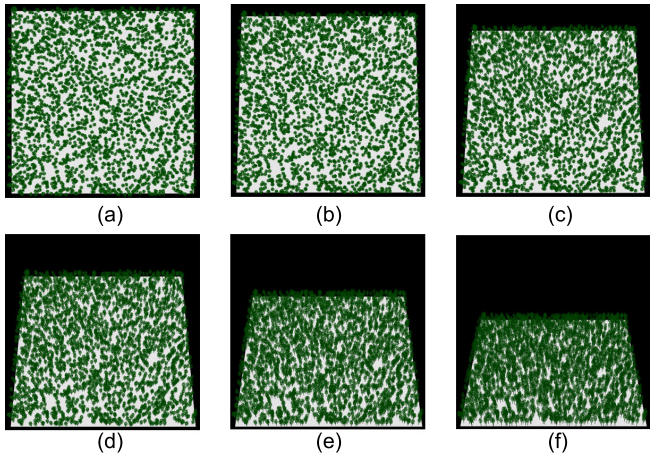

Fig. 3. Snow-covered forest scenes simulated by LESS at different view zenith angles (θ_v). (a) $\theta_v = 0°$. (b) $\theta_v = 10°$. (c) $\theta_v = 20°$. (d) $\theta_v = 30°$. (e) $\theta_v = 40°$. (f) $\theta_v = 50°$.

Evaluating the simulation performance of SFBR2 on CIS by the 3-D model is difficult because the scenario established by the LESS involves full snow cover on the land surface and no intercepted snow on the canopy. Therefore, we carried out an aerial campaign to further validate the bidirectional reflectance of forests with CIS. Three experimental sites of 50 × 50 m in flat terrain were selected from Lesser Khingan Mountains, Northeast China [Fig. 4(b)], where there is a wide distribution of coniferous forests (Korean pine), and its snow season persists for more than half a year. The field experiments were conducted on January 12, 2024, for site 1; January 6, 2024, for site 2; and January 12, 2024, for site 3 because both understory and canopy have partial snow cover and the weather is clear.

A DJI M3M UAV was used to acquire multiangular multispectral images. The equipped camera records four spectral bands at 560 nm, 650 nm (red), 730 nm, and 860 nm (NIR). Before the field experiment, we predesigned the waypoint and pitch angle in the principal plane (PP) based on the flight time, flight altitude, and target position. The view zenith angles of UAV with a 10° interval are from −60° to +60° in the PP and the distance between drone and target point was set to 200 m. During the UAV flight, the camera automatically captured multispectral images based on the waypoint flight

$$\begin{bmatrix} T_d^c & R_b^c \\ R_t^c & T_u^c \end{bmatrix} = \begin{bmatrix} \tau_{ss}^c & 0 & 0 & 0 \\ \tau_{sd}^c & \tau_{dd}^c & \rho_{dd}^c & 0 \\ \rho_{sd}^c & \rho_{dd}^c & \tau_{dd}^c & 0 \\ \rho_{so}^c & \rho_{do}^c & \tau_{do}^c & \tau_{oo}^c \end{bmatrix} = \begin{bmatrix} C_s \tau_{ss}^{c'} + (1 - C_s) & 0 & 0 & 0 \\ C_s \tau_{sd}^{c'} & C_v \tau_{dd}^{c'} + (1 - C_v) & C_v \rho_{dd}^{c'} & 0 \\ C_s \rho_{sd}^{c'} & C_v \rho_{dd}^{c'} & C_v \tau_{dd}^{c'} + (1 - C_v) & 0 \\ (1 - F_{os}) \rho_{so}^{c'} & C_o \rho_{do}^{c'} & C_o \tau_{do}^{c'} & C_o \tau_{oo}^{c'} + (1 - C_o) \end{bmatrix} \quad (14)$$

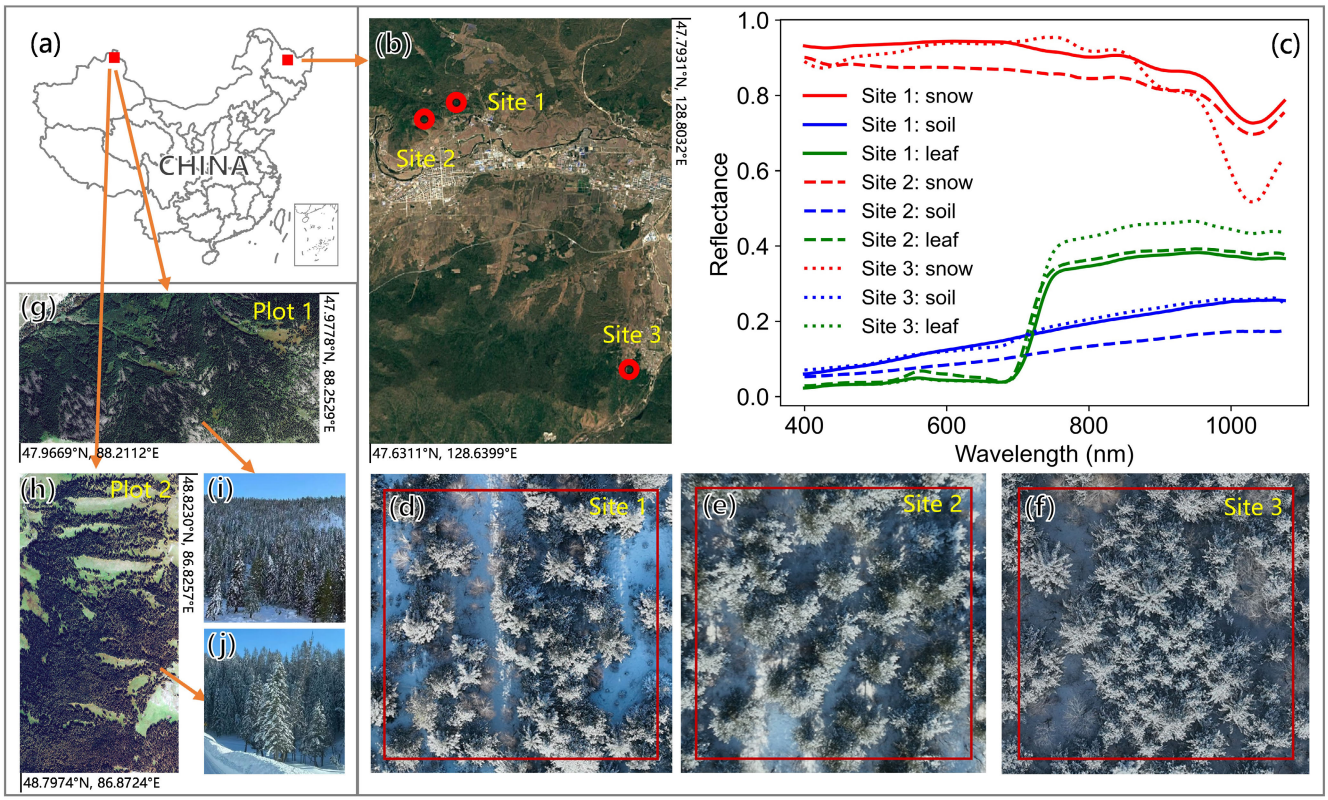

Fig. 4. Overview of the field campaign. (a) Location of the verification area. (b) Google Earth image of three experimental sites (red circles) in Lesser Khingan Mountains. (c) Average reflectance spectra of soil, leaves, and snow from multiple sampling points. (d)–(f) Nadir views of three experimental sites based on UAV RGB images, the red squares represent specific boundary ranges (50 × 50 m). (g) and (h) Google Earth images of two experimental plots in the Altai Mountains. (i) and (j) Realistic scene photos of plots 1 and 2, captured on September 28, 2023, and March 9, 2023, respectively.

mode. A total of 13 images are generated in each mission, with a spatial resolution of approximately 3 cm in the nadir direction. The UAV also captured images of reference panels, which have known reflectance and are used for radiometric calibration. Finally, the mean value of the experimental area was extracted to serve as TOC reflectance.

At the same time, the spectra of snow, soil, and leaves in the nadir direction were measured by a FieldSpec HandHeld 2 [Fig. 4(c)]. Crown diameter (d), trunk height (h_1), and tree height (h_2) were measured by a ruler and laser altimeter, TAI was measured by an LAI-2200 plant canopy analyzer (Table II). These ground gauges are mainly used to acquire input parameters for the three experimental areas. We first retrieved snow, soil, and leaf parameters via measured spectra based on an iterative optimization algorithm [74], and the optimal values were acquired by minimizing the difference between the ART, BSM, and LIBERTY simulation and measured spectra. The crown cover fraction (C_v) is determined through the supervised classification of UAV-based multispectral images. The tree shadow factor is calculated by the measured canopy structure parameters Zeta $= 2d/(h_2 + h_1)$. The other input parameters (such as FSC, thickness of CIS, dissociation factor, and SKYL) are also acquired based on an iterative optimization algorithm by comparing the SFBR2 simulation and UAV-based reflectance data.

The MODIS reflectance data are also considered observational data for model validation. Two plots of 4.5 km^2 in the Altai Mountains, Northwest China, were selected as the experimental area [Fig. 4(g) and (h)], where there is a large amount of coniferous forests (spruce, fir) and CIS was observed on September 28, 2023 (Plot 1), and March 9, 2023 (Plot 2). The MOD09GA reflectance is utilized to estimate the simulated results of SFBR2 in real snow-covered forests. Considering the absence of field-measured data, the main influential parameters (FSC, C_v, B, a_{ef}, C_{soot}, and TAI), identified through global sensitivity analysis in Section III-C1, along with SKYL and F_{CIS}, are treated as free parameters, and the other parameters are set to default values, in which C_v is obtained through a meticulous process of supervised classification and aggregation of high-resolution Google Earth images and C_{soot} is ignored because the field data show that the snow in the Altai Mountains has less pollution [75]. The remaining six parameters were inversed in the same way as for UAV verification.

B. Validation Results

1) Comparison With 3-D Model: When comparing the simulation results between the SFBR2 and 3-D LESS models, the scene is set to full snow cover on the land surface, and there is no intercepted snow in the canopy because the LESS model is unable to simulate CIS and a mixed state of snow and soil on the land surface. The same input parameters, including snow, leaf, canopy, atmosphere, and solar-target-view geometry, are used for both models. Polar plots of the TOC/TOA reflectance

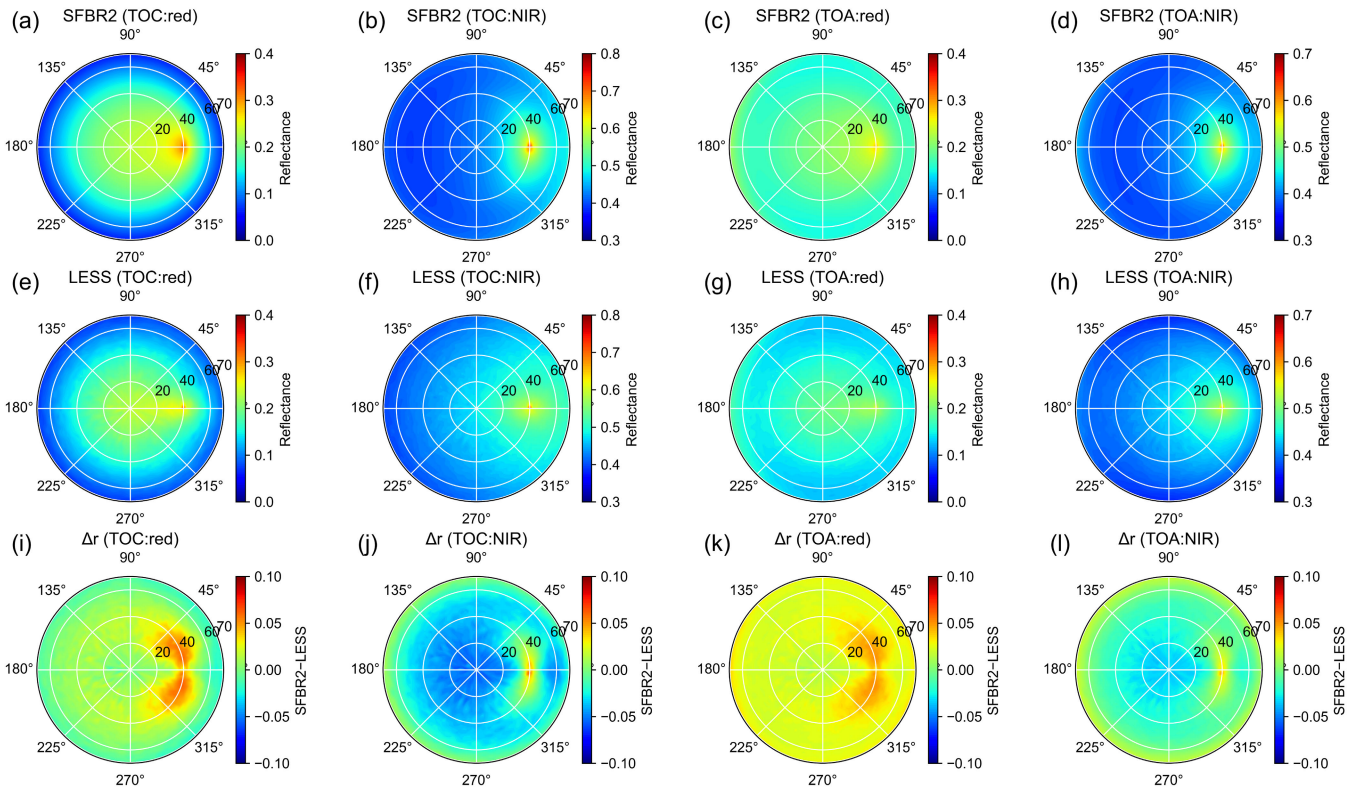

Fig. 5. Comparison of the TOC/TOA reflectance from the SFBR2 and LESS models in the hemispherical space with solar zenith angle of 40°. (a)–(d) Reflectance simulated by SFBR2 model. (e)–(h) Reflectance simulated by LESS model. (i)–(l) Reflectance difference between the SFBR2 and LESS models (Δr). Columns 1 to 4 represent the simulated TOC reflectance in the red band, TOC reflectance in the NIR band, TOA reflectance in the red band, and TOA reflectance in the NIR band, respectively.

at wavelengths of 650 nm (red) and 860 nm (NIR) with the default parameters (Table I) are shown in Fig. 5.

Compared with the LESS-simulated results, the SFBR2 results exhibit similar reflectance variations in hemispherical space. The difference of simulated reflectance is also consistent in TOC and TOA. The reflectance difference of red band is larger than that NIR band, and the difference increases as the view zenith angle increases. This is mainly because the atmosphere has more effects on the visible than on the NIR reflectance. Meanwhile, SFBR2 overestimates the red reflectance near the hotspots. This is because the radiance contribution of the shaded surface of the crowns is not fully considered in 4SAIL2. Specifically, the difference of simulated reflectance between the SFBR2 and LESS model in TOC/TOA reflectance is 0.010/0.025 and −0.034/−0.017 for the red and NIR bands, respectively [Fig. 5(i)–(l)].

Furthermore, the TOC/TOA reflectance simulated by LESS, SFBR2, and SFBR in the PP with different scenes is shown in Fig. 6. In contrast to the SFBR models, SFBR2 eliminates the need for assumptions about canopy shape and offers a flexible simulation of reflective matrix at TOC. In addition, it exhibits higher computational efficiency than the 3-D LESS model. The parameter settings include default values and change only one key parameter (vertical crown cover fraction, LAI, snow grain size, concentration of soot pollution, and aerosol optical thickness at 550 nm) from Table I. The TOC reflectance of the red band simulated by the three models has similar shapes in the PP, but SFBR has obvious underestimations at a low crown cover fraction ($C_v = 0.35$); this underestimation was also reported in the previous study [15]. In the NIR band, SFBR and SFBR2 have good consistency with the LESS-simulated TOC reflectance. Moreover, the coefficient of determination (R^2) and the root-mean-square error (RMSE) are used to estimate the model accuracy (Table III). SFBR2 shows the best accuracy with LESS for TOC reflectance simulation, with R^2 values of 0.984/0.943 and RMSE of 0.022/0.046 in the red/NIR band. SFBR only has the ability to simulate TOC reflectance. Thus, the comparison of TOA reflectance in Fig. 6 is limited to the SFBR2 and LESS models, for which R^2 and RMSE are 0.948/0.931 and 0.024/0.025, respectively, in the red/NIR band. In summary, the SFBR2 model more accurately simulates the TOC reflectance of snow-covered forests than other models and has more functions in simulating TOA reflectance.

TABLE II
FIELD MEASUREMENTS IN THREE EXPERIMENTAL SITES

	Canopy cover	TAI	Tree height (m)	Trunk height (m)	Crown Diameter (m)	Thickness of CIS (mm)
Site 1	0.64	2.26	13.92	1.47	4.61	15
Site 2	0.67	3.13	17.17	1.79	4.92	12
Site 3	0.80	3.25	15.53	8.75	3.56	7

2) Comparison With UAV and MODIS Data: The UAV observations at the three experimental sites are compared with

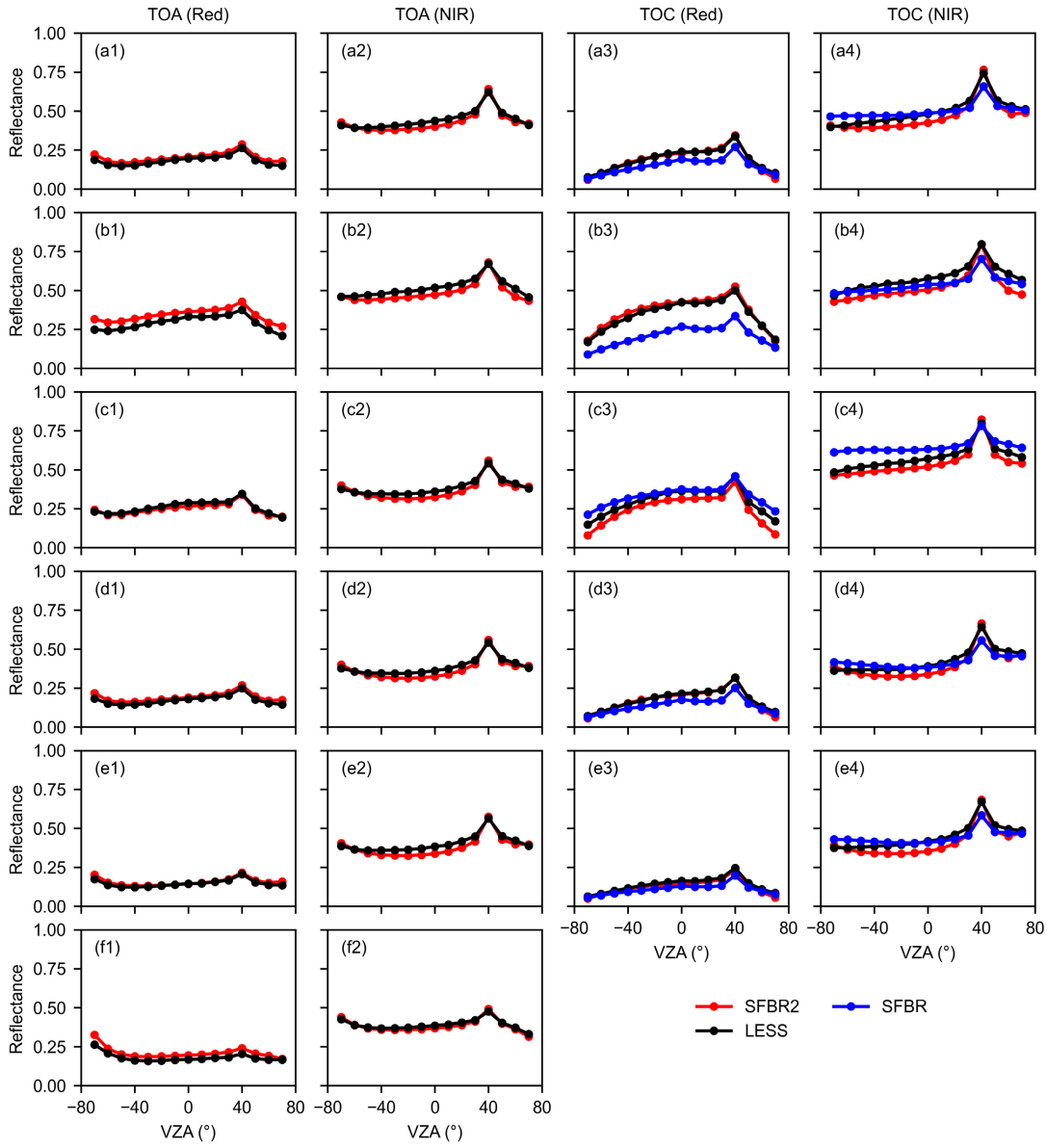

Fig. 6. Comparisons of the TOC/TOA reflectance simulated by the SFBR, SFBR2, and LESS models in the principal plane with solar zenith angle of 40°. (a1)–(a4) Simulated reflectance based on the default parameters in Table I. (b1)–(b4) Simulated reflectance with only C_v changed to 0.35. (c1)–(c4) Simulated reflectance with only LAI changed to 2.5. (d1)–(d4) Simulated reflectance with only a_{ef} changed to 2000 μm. (e1)–(e4) Simulated reflectance with only C_{soot} changed to 2000 ppb. (f1) and (f2) Simulated reflectance with only AOD changed to 0.8. Columns 1 to 4 represent the simulated TOA reflectance in the red band, TOA reflectance in the NIR band, TOC reflectance in the red band, and TOC reflectance in the NIR band, respectively.

TABLE III
STATISTICAL RESULTS OF COMPARING SIMULATED REFLECTANCE FROM THE TWO MODELS AND LESS

		Red		NIR	
		R^2	RMSE	R^2	RMSE
SFBR	TOC	0.970	0.060	0.920	0.049
SFBR2	TOC	0.984	0.022	0.943	0.046
	TOA	0.948	0.024	0.931	0.025

the simulated TOC reflectance in Fig. 7. The results reveal significant underestimations of red and NIR reflectance in the SFBR model (blue dots in Fig. 7), with R^2/RMSE values of 0.626/0.352 and 0.577/0.227 (blue dots in Fig. 8), because SFBR does not have the ability to simulate the effects of CIS. The SFBR2 model further enhances the reflectance simulation performance in snow-covered forests, demonstrating strong agreement for red and NIR reflectance in the PP when compared with UAV reflectance (red dots in Fig. 7), with R^2/RMSE values of 0.934/0.020 and 0.891/0.022 (red dots in Fig. 8). The disparities between SFBR2 and SFBR could be attributed to the increase of reflectance associated with the appearance of CIS in forested areas.

When comparing SFBR2 simulations and MODIS data, the reflectance in plots 1 and 2 agreed well in most bands, with R^2/RMSE values of 0.953/0.024 and 0.948/0.040 [Fig. 9(a) and (b)], respectively. However, the simulated results underestimate the reflectance of band 5 in plot 2, and the reason may be attributed to the interference of branches and trunks in the canopy, which have different reflective features and are not considered in the SFBR2 model.

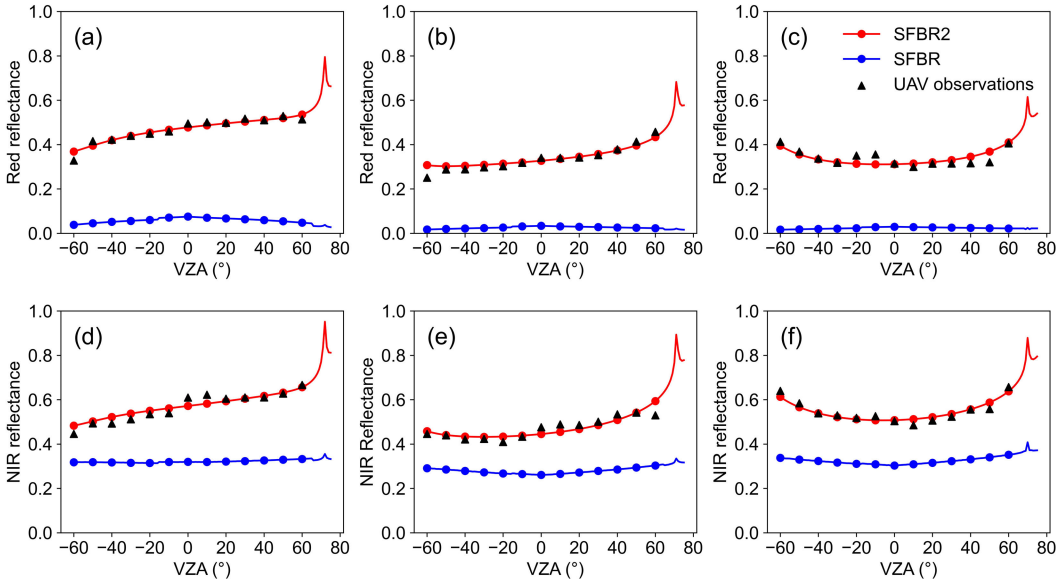

Fig. 7. Comparison of UAV reflectance and simulated reflectance at site 1 (a) and (d), site 2 (b) and (e), and site 3 (c) and (f). The solar zenith angles at the three experimental sites are 71.82°, 71.19°, and 70.01°, respectively.

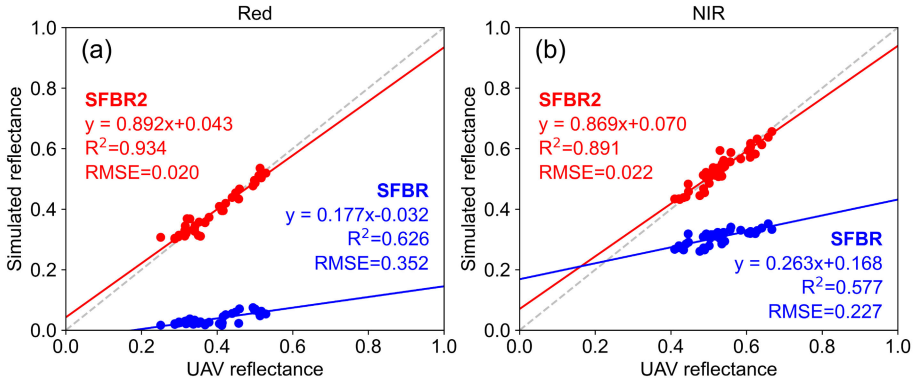

Fig. 8. Scatter plots between the simulated reflectance and UAV observations in the red (a) and NIR (b) bands.

The simulation results from SFBR show a larger bias, with R^2/RMSE values of 0.596/0.081 and 0.741/0.106 in plots 1 and 2 [Fig. 9(c) and (d)], respectively. All the validations by UAV and MODIS data jointly confirm that the SFBR2 model has a strong capability to simulate reflectance in snow-covered forests and that considering CIS can effectively improve simulation accuracy.

C. Sensitivity Analysis

1) Global Sensitivity Analysis: Sensitivity analysis of SFBR2 model is vital for model application and parameter retrieval in snow-covered forests, which can effectively quantify how much each parameter contributes to reflectance. The extension of Fourier amplitude sensitivity testing (EFAST) is a global sensitivity analysis tool that is widely used to analyze mechanistic models [76], [77] and has stable sensitivity results [78]. Thus, we use the EFAST method to calculate the total-order sensitivity index (TSI) and determine the sensitive parameters. The ranges of the parameters are shown in Table I.

MODIS bands 1–7 are selected to interpret the sensitivity of the TOC/TOA nadir reflectance to all the parameters. The center wavelengths of the selected bands are 470, 555, 650, 860, 1240, 1640, and 2130 nm. The TSI results for the different bands and the main influential parameters are shown in Fig. 10 and Table IV. For TOC reflectance, FSC, C_v, B, a_{ef}, C_{soot}, and TAI are the six most influential parameters. The FSC and C_v have the highest sensitivity indices, revealing that land cover has a significant impact on reflectivity. Meanwhile, the structural parameters (such as FSC, C_v, and TAI) are sensitive in all seven bands, but the characteristic parameters (such as B, a_{ef}, and C_{soot}) are sensitive in partial bands, which is conducive to establish a multiobjective inversion strategy for snow-covered forests. For TOA reflectance, FSC, C_v, B, AOD, a_{ef}, and C_{soot} are the six most influential parameters. The impact of AOD on snow-covered forest reflectance is mainly concentrated in the visible and NIR bands.

BRDF of snow-covered forests can be well simulated by the SFBR2 model in hemispherical space. Thus, in-depth analysis of the effects of solar-view geometry is also important for future parameter retrieval. Here, we plot the sum of the TSI over all the parameters in the different solar and viewing directions (Fig. 11). In general, the sum of TSI over all parameters

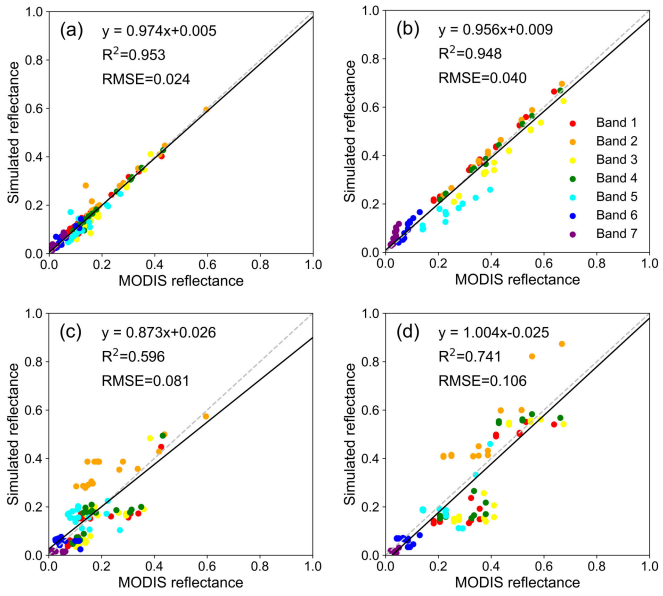

Fig. 9. Comparison of simulated reflectance and MODIS reflectance using (a) and (b) SFBR2, and (c) and (d) SFBR. The first and second columns represent plots 1 and 2, respectively.

TABLE IV
MAIN INFLUENTIAL PARAMETERS AND MEAN TSI FOR THE SEVEN MODIS BANDS

Sensitivity ranking		1	2	3	4	5	6
TOC	Parameters	FSC	C_v	B	a_{ef}	C_{soot}	TAI
	Mean of TSI	0.374	0.238	0.161	0.135	0.088	0.077
TOA	Parameters	FSC	C_v	B	AOD	a_{ef}	C_{soot}
	Mean of TSI	0.359	0.175	0.170	0.165	0.126	0.069

in TOC and TOA reflectance has similar values in the visible band and the smallest value in the NIR band. Meanwhile, the sum of TSI increases with the increase of wavelength in the shortwave infrared band. A possible explanation is that the visible band has similar sensitivities to all parameters, and the NIR band is sensitive to a few influential parameters in snow-covered forests. Moreover, as the view zenith angle increases, the sum of TSI also increases in different bands, which indicates that parameter inversion based on large view zenith angles has greater uncertainty.

2) Sensitivity to Snow and Atmosphere Parameters: Global sensitivity analysis reveals the contributions of different parameters to snow-covered forest reflectance. The key parameters of snow and atmosphere are further analyzed based on single-factor experiments. Specifically, we analyze the reflectance sensitivity to FSC, fractional CIS (F_{CIS}), and aerosol optical depth (AOD) at 550 nm under different canopy conditions, which include low and high crown cover fractions with C_v equal to 0.35 and 0.55, respectively. The other undeclared parameters are set as in Table I.

The dependence of the TOC reflectance on the FSC in the PP is shown in Fig. 12. In the red band, the BRDF changes from a slight dome shape to a typical dome shape when the FSC is increased from 0 to 0.8. However, the BRDF in the NIR band changes from a typical bowl shape to a slight bowl shape as the FSC increases. This indicates that the forward scattering of snow significantly affects the reflectance of snow-covered forests. Compared with that of high crown cover, the reflectance change with FSC has a greater amplitude in low crown cover because the contribution of snow becomes dominant in sparse canopy.

The effects of CIS on TOC reflectance are shown in Fig. 13, where the land surface has full snow cover. CIS significantly affects red reflectance, while it has a weak impact on NIR reflectance. In a sparse canopy, the average difference of red reflectance in the PP can reach 0.24 when the fractional CIS is increased from 0 to 0.8 [Fig. 13(a)], and the average difference in NIR reflectance is only 0.08 [Fig. 13(b)]. A dense canopy has a greater reflectance difference in the PP when CIS appears because a dense canopy can intercept more snow under natural conditions.

The sensitivity of the TOA reflectance to the AOD at 550 nm is shown in Fig. 14. In the red band, the reflectance decreases with increasing AOD at small view zenith angles, but the opposite trend occurs at large zenith angles because the path length of light in the atmosphere is larger at large zenith angles, and the contribution of atmospheric reflectance is strengthened in this part. In the NIR band, the TOA reflectance decreases in the PP as the AOD increases. The different performances in the red and NIR bands indicate that the atmospheric effects are more sensitive to low-reflection bands.

IV. DISCUSSION

A. CIS and Atmospheric Effects

Unlike ground snow, CIS has a limited thickness and is fully exposed to the air, which drastically alters the surface albedo [4] and hydrological processes [79]. Up to now, understanding and quantifying the effects of CIS on satellite reflectivity are still lacking. In this study, SFBR2 combines the ISIOP snow parameterization scheme [48] and two-stream theory [51] to simulate the reflectance/transmittance of CIS. When snow persists on the canopy, some leaf reflectance/transmittance is substituted by CIS; then, the radiative transfer process of canopy with snow and leaves was simulated by the 4SAIL2 model [37].

After the simulation and analysis of CIS, we found that not considering CIS resulted in a significant underestimation of snow-covered forest reflectance in the visible and NIR bands (Figs. 7 and 8). A previous study on albedo simulation also has similar conclusions [22], which revealed that ignoring CIS has significant uncertainties in snow-covered forests. The global sensitivity analysis revealed that the contribution of CIS to reflectance is lower than ground snow, and the latter has the most pronounced impact (Fig. 10). This conclusion is based on an analysis of the gradually transitioning environment from a soil-canopy system to a snow–canopy system, which can represent the sensitivity of parameters in the global terrestrial environment to reflectance. However, for most forested regions situated between 45°N and 65°N, snow fully covers the ground surface during the winter, in which CIS significantly changed

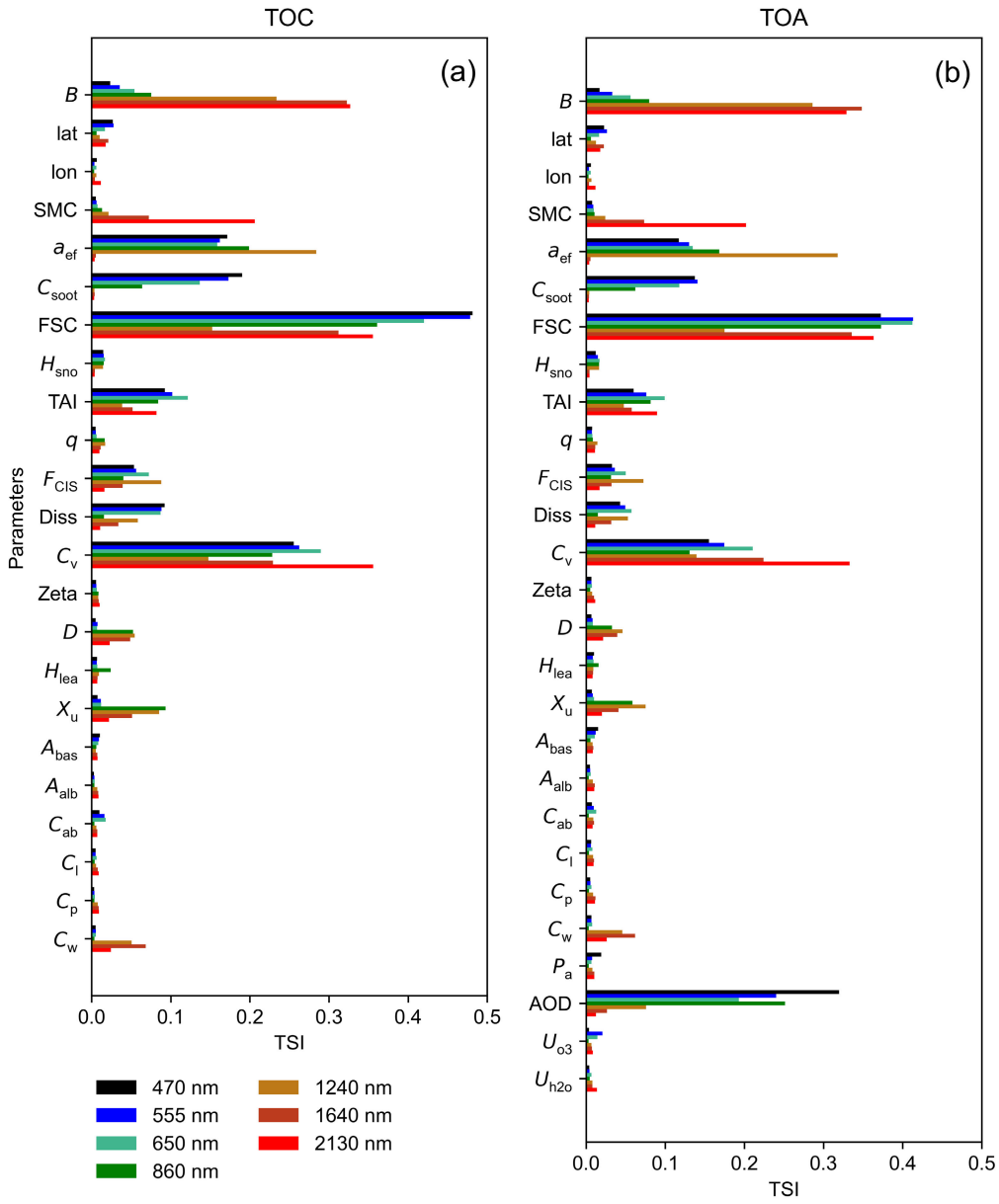

Fig. 10. Total-order sensitivity index (TSI) of the nadir TOC (a) and TOA (b) reflectance in seven MODIS bands.

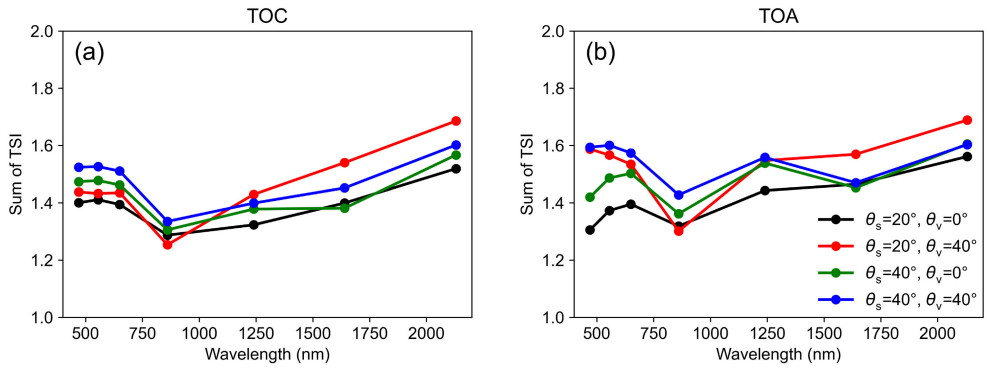

Fig. 11. Sum of TSI over all parameters for different solar zenith angle (θ_s) and view zenith angle (θ_v) in the TOC (a) and TOA (b) simulations.

the reflectivity compared with snow-free canopy (Fig. 13), and the sensitivity of the red band is greater than that of the NIR band.

The atmospheric effects are forward-modeled by the SMAC model in our study, which separates diffuse and direct transmittances to couple with non-Lambertian surfaces. The

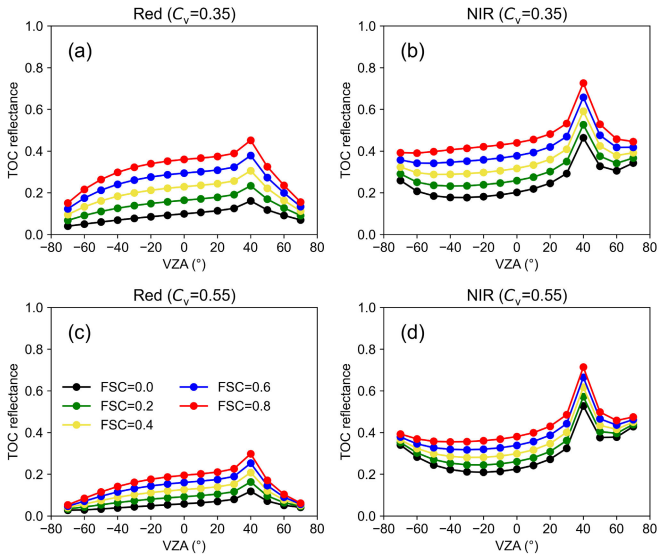

Fig. 12. Sensitivity of TOC reflectance to FSC with different crown cover fractions (C_v) in the principal plane. (a) and (b) Simulated reflectance in the red and NIR bands with $C_v = 0.35$. (c) and (d) Simulated reflectance in the red and NIR bands with $C_v = 0.55$.

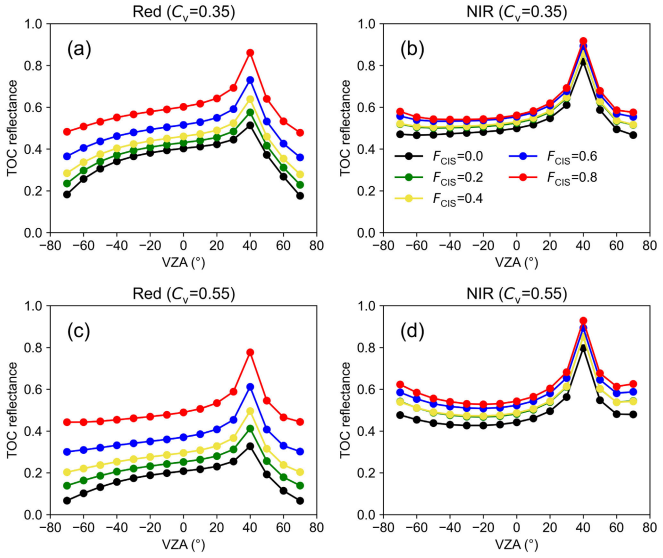

Fig. 13. Sensitivity of TOC reflectance to fractional canopy-intercepted snow (F_{CIS}) with different crown cover fractions (C_v) in the principal plane. (a) and (b) Simulated reflectance in the red and NIR bands with $C_v = 0.35$. (c) and (d) Simulated reflectance in the red and NIR bands with $C_v = 0.55$.

forward modeling process involving surface BRDF and atmosphere can be combined by the four-stream theory. Previous studies usually assumed a Lambertian surface for atmospheric correction, which may cause significant systematic errors in surface reflectance inversion [80], [81]. The SFBR2 model can avoid the process of atmospheric correction and enable direct inversion of surface parameters from TOA reflectance. Moreover, good consistency with the LESS simulation ensures model effectiveness (Fig. 6).

B. Model Limitations and Applications

The existing snow-covered forest models, such as zeroth-order radiative transfer model [25], coupling snow and GORT model [31], [32], and SFBR model [15], often assume

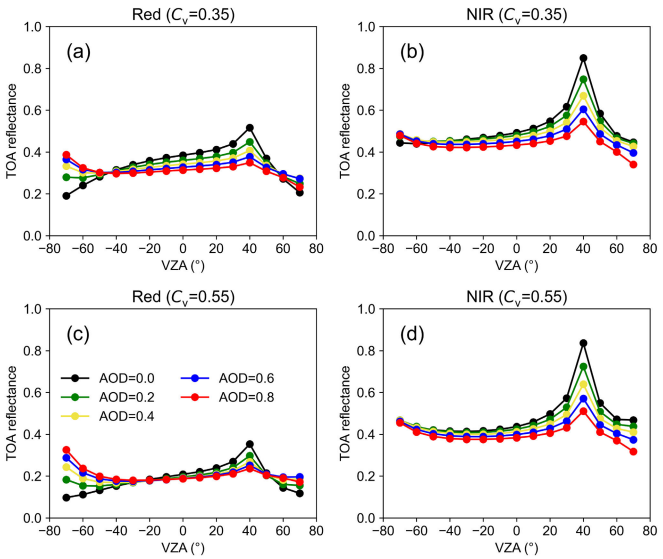

Fig. 14. Sensitivity of TOA reflectance to aerosol optical depth at 550 nm with different crown cover fractions (C_v) in the principal plane. (a) and (b) Simulated reflectance in the red and NIR bands with $C_v = 0.35$. (c) and (d) Simulated reflectance in the red and NIR bands with $C_v = 0.55$.

that snow is distributed only on the land surface and mainly focus on TOC reflectance simulation. In this study, the SFBR2 model was proposed to address the complex radiative transfer process in snow-covered forests containing different components. To our knowledge, SFBR2 is the first BRDF model for snow-covered forests with considering CIS and atmospheric effects. Validation by 3-D models, UAV observations, and MODIS data indicated that SFBR2 has good accuracy for TOC/TOA reflectance simulation.

Nevertheless, limitations and uncertainties also exist in this modeling framework.

1) The model neglects the branches of forests, which may cause some errors when deciduous forests (such as birch) persist in snow-covered forests [17]; thus, further efforts on the radiation transfer of wood elements in canopy [71], [82] are beneficial for improving model accuracy.
2) The model assumes that the ground is composed of FSC and soil, without treating the ground snow as a medium layer with a certain thickness. Solar radiation can only be reflected by ground snow and cannot penetrate it, which may introduce errors for thin snow cover. Meanwhile, considering running speed and flexibility, the ART model and combined BSM-Walthall model are currently used for simulating the BRDF of snow and soil. It is worth further exploring the integration of more effective snow or soil models, such as the improved ART model [60] and Hapke model [83], [84], for snow-covered forests.
3) The lack of terrain modeling in SFBR2 may cause radiometric distortion in mountainous areas. A solo slope assumption is an effective strategy for addressing terrain effects with high-resolution data, which involves several core steps such as topographic transformation, crown shape transformation, and leaf angle resimulation [85], [86]. Under low-resolution data, a pixel

contains numerous solo slopes and has different microtopography features (such as subpixel reflectance property, subpixel slope, subpixel aspect, and shadow), which will influence the reflectance characteristic of the pixel overall [87], [88], [89]. Therefore, the development of a solo slope or composite slope may further improve SFBR2 simulations in snow-covered forests.

From the perspective of model application, SFBR2 achieves better accuracy than SFBR when compared with the 3-D model (Fig. 6). Moreover, SFBR2 has more functions for simulating CIS and TOA reflectance, which means that SFBR2 is an excellent tool and can be used for parameter inversion in snow-covered forests. FSC and albedo products usually have low accuracy in winter forests [4], [90] because snow complicates canopy radiative properties. SFBR2, combined with an optimization method [63], lookup table method [91], and machine learning techniques [9], has the potential to improve product retrieval accuracy based on surface reflectance or TOA reflectance data. Another application is the quantitative analysis of the radiation mechanism of snow-covered forests. For example, the impact of CIS on reflection characteristics, the main influencing factors of snow-covered forest albedo, and the uncertainties of vegetation index and snow index in snow mapping can be effectively analyzed by the SFBR2 model. Ultimately, SFBR2 emerges as a comprehensive tool not limited to snow-covered forests but can be applicable to the modeling and analysis of soil, snow-free forests, and snow surface.

V. Conclusion

In this study, the novel SFBR2 model is designed to improve the BRDF simulation of snow-covered forests in both TOC and TOA. The model not only comprehensively considers partial snow cover, snow anisotropy, and needle leaf characteristics but also first quantifies the role of canopy-interception snow and the atmosphere. According to model comparison and validation, SFBR2 achieves better accuracy than SFBR when compared with the 3-D LESS model ($R^2 \geq 0.931$ and RMSE ≤ 0.046) for the snow-free canopy, and the simulation results are consistent with UAV and MODIS reflectance ($R^2 \geq 0.891$ and RMSE ≤ 0.040) for the snow-covered canopy. Moreover, the sensitivity analysis shows that FSC and C_v are the most influential parameters for TOC/TOA reflectance, which revealed that land cover has a significant impact on reflectivity. CIS also has significant effects on snow-covered forest reflectance, and the sensitivity of red band is greater than that of NIR band. All the simulation and analysis results collectively indicate that SFBR2 provides an efficient physical tool for the quantitative analysis of radiation mechanisms and parameter inversion in snow-covered forests.

Acknowledgment

The authors are grateful to the High-Performance Computing Center, Nanjing University, for computational support.

References

[1] N. Rutter et al., "Evaluation of forest snow processes models (SnowMIP2)," *J. Geophys. Res., Atmos.*, vol. 114, no. D6, Mar. 2009.

[2] M. M. Loranty, L. T. Berner, S. J. Goetz, Y. Jin, and J. T. Randerson, "Vegetation controls on northern high latitude snow-albedo feedback: Observations and CMIP5 model simulations," *Global Change Biol.*, vol. 20, no. 2, pp. 594–606, Feb. 2014.

[3] N. Helbig et al., "Snow processes in mountain forests: Interception modeling for coarse-scale applications," *Hydrol. Earth Syst. Sci.*, vol. 24, no. 5, pp. 2545–2560, May 2020.

[4] C. Webster and T. Jonas, "Influence of canopy shading and snow coverage on effective albedo in a snow-dominated evergreen needleleaf forest," *Remote Sens. Environ.*, vol. 214, pp. 48–58, Sep. 2018.

[5] Y. Li, M. Zhao, S. Motesharrei, Q. Mu, E. Kalnay, and S. Li, "Local cooling and warming effects of forests based on satellite observations," *Nature Commun.*, vol. 6, no. 1, p. 6603, Mar. 2015.

[6] C. W. Thackeray, C. G. Fletcher, and C. Derksen, "The influence of canopy snow parameterizations on snow albedo feedback in boreal forest regions," *J. Geophys. Res., Atmos.*, vol. 119, no. 16, pp. 9810–9821, Aug. 2014.

[7] B. Seyednasrollah and M. Kumar, "Net radiation in a snow-covered discontinuous forest gap for a range of gap sizes and topographic configurations," *J. Geophys. Res., Atmos.*, vol. 119, no. 17, pp. 10–323, Sep. 2014.

[8] Q. Chang et al., "Assessing consistency of spring phenology of snow-covered forests as estimated by vegetation indices, gross primary production, and solar-induced chlorophyll fluorescence," *Agricult. Forest Meteorol.*, vol. 275, pp. 305–316, Sep. 2019.

[9] J. Luo, C. Dong, K. Lin, X. Chen, L. Zhao, and L. Menzel, "Mapping snow cover in forests using optical remote sensing, machine learning and time-lapse photography," *Remote Sens. Environ.*, vol. 275, Jun. 2022, Art. no. 113017.

[10] T. H. Painter, K. Rittger, C. McKenzie, P. Slaughter, R. E. Davis, and J. Dozier, "Retrieval of subpixel snow covered area, grain size, and albedo from MODIS," *Remote Sens. Environ.*, vol. 113, no. 4, pp. 868–879, Apr. 2009.

[11] Y. Wu, P. Xiao, X. Zhang, H. Liu, Y. Dong, and L. Feng, "Effects of snow cover on spring vegetation phenology vary with temperature gradient across the pan-arctic," *J. Geophys. Res., Biogeosci.*, vol. 128, no. 4, Apr. 2023.

[12] X. Li, A. H. Strahler, and C. E. Woodcock, "A hybrid geometric optical-radiative transfer approach for modeling albedo and directional reflectance of discontinuous canopies," *IEEE Trans. Geosci. Remote Sens.*, vol. 33, no. 2, pp. 466–480, Mar. 1995.

[13] A. Kuusk, "Canopy radiative transfer modeling," in *Comprehensive Remote Sensing*, vol. 3. Amsterdam, The Netherlands: Elsevier, 2018, pp. 9–22.

[14] S. Gao et al., "Evaluating the saturation effect of vegetation indices in forests using 3D radiative transfer simulations and satellite observations," *Remote Sens. Environ.*, vol. 295, Sep. 2023, Art. no. 113665.

[15] S. Chen et al., "Simulating snow-covered forest bidirectional reflectance by extending hybrid geometric optical–radiative transfer model," *Remote Sens. Environ.*, vol. 296, Oct. 2023, Art. no. 113713.

[16] K. Rittger, M. S. Raleigh, J. Dozier, A. F. Hill, J. A. Lutz, and T. H. Painter, "Canopy adjustment and improved cloud detection for remotely sensed snow cover mapping," *Water Resour. Res.*, vol. 56, no. 6, Jun. 2020.

[17] D. Vikhamar and R. Solberg, "Subpixel mapping of snow cover in forests by optical remote sensing," *Remote Sens. Environ.*, vol. 84, no. 1, pp. 69–82, Jan. 2003.

[18] J. Zhu, J. Shi, and Y. Wang, "Subpixel snow mapping of the Qinghai–Tibet Plateau using MODIS data," *Int. J. Appl. Earth Observ. Geoinf.*, vol. 18, pp. 251–262, Aug. 2012.

[19] K. F. Huemmrich, "The GeoSail model: A simple addition to the SAIL model to describe discontinuous canopy reflectance," *Remote Sens. Environ.*, vol. 75, no. 3, pp. 423–431, Mar. 2001.

[20] W. Wiscombe and S. Warren, "A model for the spectral albedo of snow. I: Pure snow," *J. Atmos. Sci.*, vol. 37, pp. 2712–2733, Dec. 1980.

[21] A. G. Klein, D. K. Hall, and G. A. Riggs, "Improving snow cover mapping in forests through the use of a canopy reflectance model," *Hydrolog. Processes*, vol. 12, no. 1011, pp. 1723–1744, Aug. 1998.

[22] T. Manninen and P. Stenberg, "Simulation of the effect of snow covered forest floor on the total forest albedo," *Agricult. Forest Meteorol.*, vol. 149, no. 2, pp. 303–319, Feb. 2009.

[23] E. Jääskeläinen and T. Manninen, "The effect of snow at forest floor on boreal forest albedo diurnal and seasonal variation during the melting season," *Cold Regions Sci. Technol.*, vol. 185, May 2021, Art. no. 103249.

[24] M. Rautiainen and P. Stenberg, "Application of photon recollision probability in coniferous canopy reflectance simulations," *Remote Sens. Environ.*, vol. 96, no. 1, pp. 98–107, May 2005.

[25] J. Pulliainen, M. Salminen, K. Heinilä, J. Cohen, and H.-R. Hannula, "Semi-empirical modeling of the scene reflectance of snow-covered boreal forest: Validation with airborne spectrometer and LiDAR observations," *Remote Sens. Environ.*, vol. 155, pp. 303–311, Dec. 2014.

[26] S. J. Metsämäki, S. T. Anttila, H. J. Markus, and J. M. Vepsäläinen, "A feasible method for fractional snow cover mapping in boreal zone based on a reflectance model," *Remote Sens. Environ.*, vol. 95, no. 1, pp. 77–95, Mar. 2005.

[27] S. Metsämäki, O.-P. Mattila, J. Pulliainen, K. Niemi, K. Luojus, and K. Böttcher, "An optical reflectance model-based method for fractional snow cover mapping applicable to continental scale," *Remote Sens. Environ.*, vol. 123, pp. 508–521, Aug. 2012.

[28] S. Jacquemoud, S. L. Ustin, J. Verdebout, G. Schmuck, G. Andreoli, and B. Hosgood, "Estimating leaf biochemistry using the PROSPECT leaf optical properties model," *Remote Sens. Environ.*, vol. 56, no. 3, pp. 194–202, Jun. 1996.

[29] W. Ni, X. Li, C. E. Woodcock, M. R. Caetano, and A. H. Strahler, "An analytical hybrid GORT model for bidirectional reflectance over discontinuous plant canopies," *IEEE Trans. Geosci. Remote Sens.*, vol. 37, no. 2, pp. 987–999, Mar. 1999.

[30] W. Ni and C. E. Woodcock, "Effect of canopy structure and the presence of snow on the albedo of boreal conifer forests," *J. Geophys. Res., Atmos.*, vol. 105, no. D9, pp. 11879–11888, May 2000.

[31] G. Wang, L. Jiang, C. Xiong, and Y. Zhang, "Characterization of NDSI variation: Implications for snow cover mapping," *IEEE Trans. Geosci. Remote Sens.*, vol. 60, 2022.

[32] Q. Xin, C. E. Woodcock, J. Liu, B. Tan, R. A. Melloh, and R. E. Davis, "View angle effects on MODIS snow mapping in forests," *Remote Sens. Environ.*, vol. 118, pp. 50–59, Mar. 2012.

[33] C. Xiong, J. Shi, D. Ji, T. Wang, Y. Xu, and T. Zhao, "A new hybrid snow light scattering model based on geometric optics theory and vector radiative transfer theory," *IEEE Trans. Geosci. Remote Sens.*, vol. 53, no. 9, pp. 4862–4875, Sep. 2015.

[34] T. P. Dawson, P. J. Curran, and S. E. Plummer, "LIBERTY—Modeling the effects of leaf biochemical concentration on reflectance spectra," *Remote Sens. Environ.*, vol. 65, no. 1, pp. 50–60, Jul. 1998.

[35] A. A. Kokhanovsky and E. P. Zege, "Scattering optics of snow," *Appl. Opt.*, vol. 43, no. 7, p. 1589, 2004.

[36] W. Fan, J. M. Chen, W. Ju, and N. Nesbitt, "Hybrid geometric optical–radiative transfer model suitable for forests on slopes," *IEEE Trans. Geosci. Remote Sens.*, vol. 52, no. 9, pp. 5579–5586, Sep. 2014.

[37] W. Verhoef and H. Bach, "Coupled soil-leaf-canopy and atmosphere radiative transfer modeling to simulate hyperspectral multi-angular surface reflectance and TOA radiance data," *Remote Sens. Environ.*, vol. 109, no. 2, pp. 166–182, Jul. 2007.

[38] J. Qi et al., "LESS: Large-scale remote sensing data and image simulation framework over heterogeneous 3D scenes," *Remote Sens. Environ.*, vol. 221, pp. 695–706, Feb. 2019.

[39] M. S. Raleigh, E. D. Gutmann, J. T. Van Stan, S. P. Burns, P. D. Blanken, and E. E. Small, "Challenges and capabilities in estimating snow mass intercepted in conifer canopies with tree sway monitoring," *Water Resour. Res.*, vol. 58, no. 3, Mar. 2022.

[40] P. Storck, D. P. Lettenmaier, and S. M. Bolton, "Measurement of snow interception and canopy effects on snow accumulation and melt in a mountainous maritime climate, Oregon, United States," *Water Resour. Res.*, vol. 38, no. 11, pp. 5-1–5-16, Nov. 2002.

[41] M. Stähli, T. Jonas, and D. Gustafsson, "The role of snow interception in winter-time radiation processes of a coniferous subalpine forest," *Hydrolog. Processes*, vol. 23, no. 17, pp. 2498–2512, Aug. 2009.

[42] Z. Lv and J. W. Pomeroy, "Detecting intercepted snow on mountain needleleaf forest canopies using satellite remote sensing," *Remote Sens. Environ.*, vol. 231, Sep. 2019, Art. no. 111222.

[43] A. S. Gardner and M. J. Sharp, "A review of snow and ice albedo and the development of a new physically based broadband albedo parameterization," *J. Geophys. Res., Earth Surf.*, vol. 115, no. F1, Mar. 2010, Art. no. F01009.

[44] P. Yang, C. van der Tol, T. Yin, and W. Verhoef, "The SPART model: A soil-plant-atmosphere radiative transfer model for satellite measurements in the solar spectrum," *Remote Sens. Environ.*, vol. 247, Sep. 2020, Art. no. 111870.

[45] A. A. Kokhanovsky, T. Aoki, A. Hachikubo, M. Hori, and E. P. Zege, "Reflective properties of natural snow: Approximate asymptotic theory versus in situ measurements," *IEEE Trans. Geosci. Remote Sens.*, vol. 43, no. 7, pp. 1529–1535, Jul. 2005.

[46] W. Verhoef, C. van der Tol, and E. M. Middleton, "Hyperspectral radiative transfer modeling to explore the combined retrieval of biophysical parameters and canopy fluorescence from FLEX—Sentinel-3 tandem mission multi-sensor data," *Remote Sens. Environ.*, vol. 204, pp. 942–963, Jan. 2018.

[47] C. L. Walthall, J. M. Norman, J. M. Welles, G. Campbell, and B. L. Blad, "Simple equation to approximate the bidirectional reflectance from vegetative canopies and bare soil surfaces," *Appl. Opt.*, vol. 24, no. 3, p. 383, 1985.

[48] K. Stamnes et al., "Modeling of radiation transport in coupled atmosphere-snow-ice-ocean systems," *J. Quant. Spectrosc. Radiat. Transf.*, vol. 112, no. 4, pp. 714–726, Mar. 2011.

[49] E. Zege, I. Katsev, A. Malinka, A. Prikhach, and I. Polonsky, "New algorithm to retrieve the effective snow grain size and pollution amount from satellite data," *Ann. Glaciol.*, vol. 49, no. 1, pp. 139–144, 2008.

[50] Q. Libois et al., "Experimental determination of the absorption enhancement parameter of snow," *J. Glaciol.*, vol. 60, no. 222, pp. 714–724, 2014.

[51] W. E. Meador and W. R. Weaver, "Two-stream approximations to radiative transfer in planetary atmospheres: A unified description of existing methods and a new improvement," *J. Atmos. Sci.*, vol. 37, no. 3, pp. 630–643, Mar. 1980.

[52] M. Dumont, O. Brissaud, G. Picard, B. Schmitt, J.-C. Gallet, and Y. Arnaud, "High-accuracy measurements of snow bidirectional reflectance distribution function at visible and NIR wavelengths—Comparison with modelling results," *Atmos. Chem. Phys.*, vol. 10, no. 5, pp. 2507–2520, Mar. 2010.

[53] C. He and M. Flanner, "Snow albedo and radiative transfer theory, modeling, and parameterization," in *Radiative Transfer, Remote Sensing, and Light Scattering* (Springer Series in Light Scattering), vol. 5. Cham, Switzerland: Springer, 2020, pp. 67–133.

[54] A. Kokhanovsky, "Spectral reflectance of solar light from dirty snow: A simple theoretical model and its validation," *Cryosphere*, vol. 7, no. 4, pp. 1325–1331, Aug. 2013.

[55] A. A. Kokhanovsky, "Reflection and polarization of light by semi-infinite turbid media: Simple approximations," *J. Colloid Interface Sci.*, vol. 251, no. 2, pp. 429–433, Jul. 2002.

[56] E. P. Zege, I. L. Katsev, A. V. Malinka, A. S. Prikhach, G. Heygster, and H. Wiebe, "Algorithm for retrieval of the effective snow grain size and pollution amount from satellite measurements," *Remote Sens. Environ.*, vol. 115, no. 10, pp. 2674–2685, Oct. 2011.

[57] A. Ångstrom, "The albedo of various surface of ground," *Geogr. Ann.*, vol. 7, no. 4, pp. 323–342, 1925.

[58] C. Jiang and H. Fang, "GSV: A general model for hyperspectral soil reflectance simulation," *Int. J. Appl. Earth Observ. Geoinf.*, vol. 83, Nov. 2019, Art. no. 101932.

[59] J. C. Price, "On the information content of soil reflectance spectra," *Remote Sens. Environ.*, vol. 33, no. 2, pp. 113–121, Aug. 1990.

[60] A. Ding, S. Liang, Z. Jiao, H. Ma, A. A. Kokhanovsky, and J. Peltoniemi, "Improving the asymptotic radiative transfer model to better characterize the pure snow hyperspectral bidirectional reflectance," *IEEE Trans. Geosci. Remote Sens.*, vol. 60, 2022.

[61] J. Peltoniemi, T. Hakala, J. Suomalainen, and E. Puttonen, "Polarised bidirectional reflectance factor measurements from soil, stones, and snow," *J. Quant. Spectrosc. Radiat. Transf.*, vol. 110, no. 17, pp. 1940–1953, Nov. 2009.

[62] T. Nilson and A. Kuusk, "A reflectance model for the homogeneous plant canopy and its inversion," *Remote Sens. Environ.*, vol. 27, no. 2, pp. 157–167, Feb. 1989.

[63] H. Ma, S. Liang, H. Shi, and Y. Zhang, "An optimization approach for estimating multiple land surface and atmospheric variables from the geostationary advanced Himawari imager top-of-atmosphere observations," *IEEE Trans. Geosci. Remote Sens.*, vol. 59, no. 4, pp. 2888–2908, Apr. 2021.

[64] 19 H. Shi, Z. Xiao, S. Liang, and X. Zhang, "Consistent estimation of multiple parameters from MODIS top of atmosphere reflectance data using a coupled soil-canopy-atmosphere radiative transfer model," *Remote Sens. Environ.*, vol. 184, pp. 40–57, Oct. 2016.

[65] S. G. Leblanc and J. M. Chen, "A windows graphic user interface (GUI) for the five-scale model for fast BRDF simulations," *Remote Sens. Rev.*, vol. 19, nos. 1–4, pp. 293–305, 2000.

[66] J. Dash and P. J. Curran, "The MERIS terrestrial chlorophyll index," *Int. J. Remote Sens.*, vol. 25, no. 23, pp. 5403–5413, Dec. 2004.

[67] A. Rosema, W. Verhoef, H. Noorbergen, and J. J. Borgesius, "A new forest light interaction model in support of forest monitoring," *Remote Sens. Environ.*, vol. 42, no. 1, pp. 23–41, Oct. 1992.

[68] H. Rahman and G. Dedieu, "SMAC: A simplified method for the atmospheric correction of satellite measurements in the solar spectrum," *Int. J. Remote Sens.*, vol. 15, no. 1, pp. 123–143, Jan. 1994.

[69] E. F. Vermote, D. Tanre, J. L. Deuze, M. Herman, and J.-J. Morcette, "Second simulation of the satellite signal in the solar spectrum, 6S: An overview," *IEEE Trans. Geosci. Remote Sens.*, vol. 35, no. 3, pp. 675–686, May 1997.

[70] W. Verhoef, L. Jia, Q. Xiao, and Z. Su, "Unified optical-thermal four-stream radiative transfer theory for homogeneous vegetation canopies," *IEEE Trans. Geosci. Remote Sens.*, vol. 45, no. 6, pp. 1808–1822, Jun. 2007.

[71] C. Niu, W. Woodgate, S. R. Phinn, C. M. Roelfsema, and Y. Su, "Extending a canopy reflectance model for mangroves: A case study in South East Queensland, Australia," *Agricult. Forest Meteorol.*, vol. 316, Apr. 2022, Art. no. 108875.

[72] Z. Bian et al., "A TIR forest reflectance and transmittance (FRT) model for directional temperatures with structural and thermal stratification," *Remote Sens. Environ.*, vol. 268, Jan. 2022, Art. no. 112749.

[73] J. Geng et al., "Application of a hypergeometric model in simulating canopy gap fraction and BRF for forest plantations on sloping terrains," *IEEE J. Sel. Topics Appl. Earth Observ. Remote Sens.*, vol. 15, pp. 2901–2913, Mar. 2022.

[74] J.-B. Féret, A. A. Gitelson, S. D. Noble, and S. Jacquemoud, "PROSPECT-D: Towards modeling leaf optical properties through a complete lifecycle," *Remote Sens. Environ.*, vol. 193, pp. 204–215, May 2017.

[75] H. Ye, R. Zhang, J. Shi, J. Huang, S. G. Warren, and Q. Fu, "Black carbon in seasonal snow across northern Xinjiang in northwestern China," *Environ. Res. Lett.*, vol. 7, no. 4, Dec. 2012, Art. no. 044002.

[76] A. Mousivand, M. Menenti, B. Gorte, and W. Verhoef, "Global sensitivity analysis of the spectral radiance of a soil–vegetation system," *Remote Sens. Environ.*, vol. 145, pp. 131–144, Apr. 2014.

[77] G. Zhang, H. Ma, and S. Liang, "Estimating 250-m land surface and atmospheric variables from MERSI top-of-atmosphere reflectance," *IEEE Trans. Geosci. Remote Sens.*, vol. 60, 2022.

[78] P. A. Vanrolleghem, G. Mannina, A. Cosenza, and M. B. Neumann, "Global sensitivity analysis for urban water quality modelling: Terminology, convergence and comparison of different methods," *J. Hydrol.*, vol. 522, pp. 339–352, Mar. 2015.

[79] Z. Lv and J. W. Pomeroy, "Assimilating snow observations to snow interception process simulations," *Hydrolog. Processes*, vol. 34, no. 10, pp. 2229–2246, May 2020.

[80] S. Liang, H. Fang, and M. Chen, "Atmospheric correction of Landsat ETM+ land surface imagery. I. Methods," *IEEE Trans. Geosci. Remote Sens.*, vol. 39, no. 11, pp. 2490–2498, Aug. 2001.

[81] S. Liang et al., "Atmospheric correction of Landsat ETM+ land surface imagery. II. Validation and applications," *IEEE Trans. Geosci. Remote Sens.*, vol. 40, no. 12, pp. 2736–2746, Dec. 2002.

[82] J. Verrelst, M. E. Schaepman, Z. Malenovský, and J. G. P. W. Clevers, "Effects of woody elements on simulated canopy reflectance: Implications for forest chlorophyll content retrieval," *Remote Sens. Environ.*, vol. 114, no. 3, pp. 647–656, Mar. 2010.

[83] A. Ding, H. Ma, S. Liang, and T. He, "Extension of the Hapke model to the spectral domain to characterize soil physical properties," *Remote Sens. Environ.*, vol. 269, Feb. 2022, Art. no. 112843.

[84] G.-J. Yang, C.-J. Zhao, W.-J. Huang, and J.-H. Wang, "Extension of the Hapke bidirectional reflectance model to retrieve soil water content," *Hydrol. Earth Syst. Sci.*, vol. 15, no. 7, pp. 2317–2326, Jul. 2011.

[85] H. Shi and Z. Xiao, "The 4SAILT model: An improved 4SAIL canopy radiative transfer model for sloping terrain," *IEEE Trans. Geosci. Remote Sens.*, vol. 59, no. 7, pp. 5515–5525, Jul. 2021.

[86] S. Wu et al., "Modeling discrete forest anisotropic reflectance over a sloped surface with an extended GOMS and SAIL model," *IEEE Trans. Geosci. Remote Sens.*, vol. 57, no. 2, pp. 944–957, Feb. 2019.

[87] D. Hao et al., "Modeling anisotropic reflectance over composite sloping terrain," *IEEE Trans. Geosci. Remote Sens.*, vol. 56, no. 7, pp. 3903–3923, Jul. 2018.

[88] J. Wen et al., "Characterizing land surface anisotropic reflectance over rugged terrain: A review of concepts and recent developments," *Remote Sens.*, vol. 10, no. 3, p. 370, Feb. 2018.

[89] D. Hao, J. Wen, Q. Xiao, D. You, and Y. Tang, "An improved topography-coupled kernel-driven model for land surface anisotropic reflectance," *IEEE Trans. Geosci. Remote Sens.*, vol. 58, no. 4, pp. 2833–2847, Apr. 2020.

[90] M. S. Raleigh, K. Rittger, C. E. Moore, B. Henn, J. A. Lutz, and J. D. Lundquist, "Ground-based testing of MODIS fractional snow cover in subalpine meadows and forests of the sierra Nevada," *Remote Sens. Environ.*, vol. 128, pp. 44–57, Jan. 2013.

[91] Y. Qu, S. Liang, Q. Liu, X. Li, Y. Feng, and S. Liu, "Estimating Arctic sea-ice shortwave albedo from MODIS data," *Remote Sens. Environ.*, vol. 186, pp. 32–46, Dec. 2016.

Siyong Chen received the B.S. degree in geology from Chang'an University, Xi'an, China, in 2016, and the M.S. degree in cartography and geographic information systems from Lanzhou University, Lanzhou, China, in 2021. He is currently pursuing the Ph.D. degree with Nanjing University, Nanjing, China.

His research interests include remote sensing data reconstruction, radiative transfer/geometric optical modeling, and snow parameters retrieval.

Pengfeng Xiao (Senior Member, IEEE) received the B.M. degree in land resource management from Hunan Normal University, Changsha, China, in 2002, and the Ph.D. degree in cartography and geographical information system from Nanjing University, Nanjing, China, in 2007.

From 2007 to 2009, he was a Lecturer with the School of Geography and Ocean Science, Nanjing University, where he was an Associate Professor from 2010 to 2018. He was a Visiting Scholar with the Department of Geography, University of Giessen, Giessen, Hesse, Germany, from 2011 to 2012; and the Department of Environmental Science, Policy, and Management, University of California at Berkeley, Berkeley, CA, USA, from 2014 to 2015. Since 2019, he has been a Professor with Nanjing University. He has authored four books and over 160 articles. His research interests include high-resolution remote sensing image analysis, remote sensing of snow cover, and land use and land cover change.

Xueliang Zhang (Senior Member, IEEE) received the B.S. degree in geographical information system and the Ph.D. degree in remote sensing of resources and environment from Nanjing University, Nanjing, China, in 2010 and 2015, respectively.

From 2014 to 2015, he was a Visiting Student with the Informatics Institute, University of Missouri, Columbia, MO, USA. From 2016 to 2018, he was an Associate Researcher with the School of Geography and Ocean Science, Nanjing University, where he is currently an Associate Professor. His research interests include high-resolution remote sensing image analysis, AI for remote sensing, and remote sensing of snow.

Hao Liu received the B.S. degree in geomatics engineering from the Central South University of Forestry and Technology, Changsha, China, in 2017, and the M.S. degree in photogrammetry and remote sensing from Nanjing University, Nanjing, China, in 2020, where he is currently pursuing the Ph.D. degree in geography.

His research interests include remote sensing of snow cover, ecological, and climatic effects of snow cover.

Yunhan Wang received the B.S. degree in geographic information science from Southeast University, Nanjing, China, in 2022. She is currently pursuing the M.S. degree in cartography and geographic information system with Nanjing University, Nanjing.

Her research interests include remote sensing of snow cover and ecological effect of snow cover change.

Liyang Sun received the B.S. degree in geographic information science from the Hohai University of China, Nanjing, China, in 2022. She is currently pursuing the master's degree in cartography and geographic information systems with Nanjing University, Nanjing.

Her research interests include snow water equivalent and snow density mapping.

Gaofei Yin (Senior Member, IEEE) received the bachelor's degree from Southwest Jiaotong University, Chengdu, China, in 2008, the master's degree from Nanjing University, Nanjing, China, in 2011, and the Ph.D. degree from the Chinese Academy of Sciences, Beijing, China, in 2015.

From 2015 to 2018, he conducted Postdoctoral Research at the Institute of Mountain Hazards and Environment, Chinese Academy of Sciences, Chengdu. From 2019 to 2021, he worked as a Marie Skłodowska-Curie Individual Fellow at the Global Ecology Unit, Center for Ecological Research and Forestry Applications, Barcelona, Spain. He is currently a Professor with the Faculty of Geosciences and Engineering, Southwest Jiaotong University, Chengdu. His current research interests include vegetation remote sensing, global change ecology, and the impacts of human activities, particularly transportation behavior, on ecosystems.

Dr. Yin also serves as an Associate Editor for IEEE GEOSCIENCE AND REMOTE SENSING LETTERS.